

Technical Report
821

**A Model for the Infrared Radiance of
Optically Thin, Particulate Exhaust Plumes
Generated by Pyrotechnic Flares
Burning in a Vacuum**

D.L. Cohen

17 March 1989
Reissued 29 March 2000

Lincoln Laboratory
MASSACHUSETTS INSTITUTE OF TECHNOLOGY
LEXINGTON, MASSACHUSETTS



Prepared for the Department of the Air Force
under Electronic Systems Division Contract F19628-85-C-0002.

Approved for public release; distribution is unlimited.

DTIC QUALITY INSPECTED 3

20000404 000

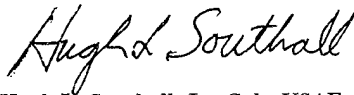
The work reported in this document was performed at Lincoln Laboratory, a center for research operated by Massachusetts Institute of Technology. This work was sponsored by the Air Force under Contract F19628-85-C-0002.

This report may be reproduced to satisfy needs of U.S. Government agencies.

The SMC Public Affairs Office has reviewed this report, and it is releasable to the National Technical Information Service, where it will be available to the general public, including foreign nationals.

This technical report has been reviewed and is approved for publication.

FOR THE COMMANDER



Hugh L. Southall, Lt. Col., USAF
Chief, ESD Lincoln Laboratory Project Office

Non-Lincoln Recipients
PLEASE DO NOT RETURN

Permission is given to destroy this document,
when it is no longer needed.

MASSACHUSETTS INSTITUTE OF TECHNOLOGY
LINCOLN LABORATORY

**A MODEL FOR THE INFRARED RADIANCE OF
OPTICALLY THIN, PARTICULATE EXHAUST PLUMES
GENERATED BY PYROTECHNIC FLARES BURNING IN A VACUUM**

D.L. COHEN
Group 95

TECHNICAL REPORT 821

17 MARCH 1989
REISSUED 29 MARCH 2000

Approved for public release; distribution is unlimited.

LEXINGTON

MASSACHUSETTS

ABSTRACT

This report sets up a model for the intensity of infrared radiation emitted by a particulate exhaust plume generated by a pyrotechnic flare burning in a vacuum. The model assumes that the exhaust plume is optically thin, that it is composed mostly of discrete particles, that the particles have a size spectrum described by a log-normal probability density function, that they cool off entirely by the emission of thermal radiation, and that they all travel at the same average velocity. The model is used to predict how a magnesium-Teflon exhaust plume would look when viewed as an approximate point source by a distant infrared sensor and also to analyze the data acquired from three separate magnesium-Teflon flares burned in a large vacuum chamber.

TABLE OF CONTENTS

Abstract	iii
List of Illustrations	vii
List of Tables	ix
1. INTRODUCTION	1
2. DERIVATION OF THE MODEL EQUATIONS	3
3. INVESTIGATION OF AN EXOATMOSPHERIC FLARE	13
4. APPLICATION OF THE MODEL TO EXPERIMENTAL DATA	27
5. CONCLUSIONS	43
References	45
Bibliography	45

LIST OF ILLUSTRATIONS

Figure No.		Page
2-1	Graph of Mie-Theory Emissivity versus $2\pi \times (\text{Particle Radius})/(\text{Radiation Wavelength})$ for Several Values of the Complex Index of Refraction n	5
2-2	Graph of Mie-Theory Emissivity versus $2\pi \times (\text{Particle Radius})/(\text{Radiation Wavelength})$ for Several Values of the Complex Index of Refraction n	5
2-3	Graph of P_l and Its Approximation P_{la} versus ξ	6
2-4	Graph of the Absolute Error Between P_l and P_{la} versus ξ	7
2-5	Steady-State Exhaust Plume Generated by a Flare Burning in a Vacuum	8
2-6	Graph of x versus q for $x_0 = 0.25, 0.50, 0.75, 1$	9
2-7	Graph of x versus q for $x_0 = 1, 2, 3, 8$	10
3-1	Three Coordinate Systems Used to Investigate How a Mg-Teflon Exhaust Plume Would Look When Viewed by a Distant IR Sensor	12
3-2	Graph of \mathcal{J} and Its Approximation \mathcal{J}_a versus x	15
3-3	Graph of the Absolute Error Between \mathcal{J} and \mathcal{J}_a versus x	16
3-4	How a Conical Exhaust Plume Intersects an Imaginary Sphere Centered on the Burning Flare	17
3-5	Transformation from the (a) Unprimed to the Primed Coordinate System; and (b) Primed to the Double-Primed Coordinate System	19
3-6	Graph of A versus u for $\theta_{\max} = 15^\circ$, $\theta_s = 0.1^\circ$, and $\theta_p = 0^\circ, 30^\circ, 60^\circ, 90^\circ$	20
3-7	Graph of A versus u for $\theta_{\max} = 30^\circ$, $\theta_s = 0.1^\circ$ and $\theta_p = 0^\circ, 30^\circ, 60^\circ, 90^\circ$	21
3-8	Graph of A versus u for $\theta_{\max} = 45^\circ$, $\theta_s = 0.1^\circ$ and $\theta_p = 0^\circ, 30^\circ, 60^\circ, 90^\circ$	21
3-9	Graph of J_λ/P versus λ for $s = 100$ km, $\theta_{\max} = 30^\circ$, $\theta_s = 0.1^\circ$, $v_o/A_e = 300$ m/s, $R_o = 1$ μm , and $L_f = 0.437$ km	22
3-10	Graph of J_λ/P versus λ for $s = 100$ km, $\theta_{\max} = 30^\circ$, $\theta_s = 0.1^\circ$, $v_o/A_e = 300$ m/s, $R_o = 10$ μm , and $L_f = 1.92$ km	23

Figure No.		Page
3-11	Graph of E_λ versus λ for $s = 100$ km, $\theta_{\max} = 15^\circ$, $\theta_s = 0.1^\circ$, $v_o/A_e = 100$ m/s, $R_o = 5$ μ m, and $L_f = 0.331$ km	24
3-12	Graph of E_λ versus λ for $s = 100$ km, $\theta_{\max} = 30^\circ$, $\theta_s = 0.1^\circ$, $v_o/A_e = 100$ m/s, $R_o = 5$ μ m, and $L_f = 0.331$ km	24
3-13	Graph of E_λ versus λ for $s = 100$ km, $\theta_{\max} = 45^\circ$, $\theta_s = 0.1^\circ$, $v_o/A_e = 100$ m/s, $R_o = 5$ μ m, and $L_f = 0.331$ km	25
3-14	Graph of E_λ versus λ for $s = 100$ km, $\theta_{\max} = 15^\circ$, $\theta_s = 0.1^\circ$, $v_o/A_e = 300$ m/s, $R_o = 5$ μ m, and $L_f = 0.994$ km	25
3-15	Graph of E_λ versus λ for $s = 100$ km, $\theta_{\max} = 30^\circ$, $\theta_s = 0.1^\circ$, $v_o/A_e = 300$ m/s, $R_o = 5$ μ m, and $L_f = 0.994$ km	26
3-16	Graph of E_λ versus λ for $s = 100$ km, $\theta_{\max} = 45^\circ$, $\theta_s = 0.1^\circ$, $v_o/A_e = 300$ m/s, $R_o = 5$ μ m, and $L_f = 0.994$ km	26
4-1	Experimental Setup Used in the March 1988 Test Series	27
4-2	Graph of C_j versus j From Burn 8 at 2.9 s After Ignition	30
4-3	Graph of C_j versus j From Burn 7 at 2.5 s After Ignition	30
4-4	Graph of the Photometer Signal (10-cm Station) versus Time for Burns 6, 7, and 8	32
4-5	Graph of Average Radiant Intensity versus Distance Down the Plume for Burn 6	37
4-6	Graph of Average Radiant Intensity versus Distance Down the Plume for Burn 7	38
4-7	Graph of Average Radiant Intensity versus Distance Down the Plume for Burn 8	39

LIST OF TABLES

Table No.		Page
4-1	Average Velocities From Photometer Correlations Over Intervals of 0.107 s	31
4-2	Average Radiance Values Versus Distance Down the Plume for Burn 6 of March 1988 Test Series	33
4-3	Average Radiance Values Versus Distance Down the Plume for Burn 7 of March 1988 Test Series	34
4-4	Average Radiance Values Versus Distance Down the Plume for Burn 8 of March 1988 Test Series	35
4-5	Comparison of Inframetrics Radiometer Channel 1 Readings to 91-cm Station Photometer for March 1988 Test Series	40
4-6	Comparison of Inframetrics Radiometer Channel 2 Readings to 91-cm Station CVF Spectrometer for March 1988 Test Series	41

A MODEL FOR THE INFRARED RADIANCE OF OPTICALLY THIN, PARTICULATE EXHAUST PLUMES GENERATED BY PYROTECHNIC FLARES BURNING IN A VACUUM

1. INTRODUCTION

For the last two years the Air Force has sponsored work in Group 95 at Lincoln Laboratory aimed at understanding the characteristics of infrared (IR) radiation emitted from the exhaust plumes of pyrotechnic flares burning in a vacuum. Over this period of time, a model has been developed which has proven to be reasonably successful at explaining the results of laboratory experiments. This model assumes that the vacuum exhaust plumes are optically thin, that they are composed mostly of particles, and that the particles cool off entirely by the emission of thermal radiation as they travel down the plume. The particles are assumed to come in a variety of sizes, with a size distribution which obeys a log-normal probability density function, and to travel at the same average velocity. The model will work for any exhaust plume composed primarily of discrete particles, but it has been applied here only to Mg-Teflon flares, because working with this type of pyrotechnic proved to be experimentally convenient.

Following this introduction, Section 2 outlines the mathematical development of the model equations and describes the basic approximations that went into their derivation. In particular, a phenomenological approximation (instead of Mie theory) is used to describe the variation of exhaust particle grey-body emissivity with particle size, allowing the model to acknowledge both the geometric irregularity and the lack of chemical purity of the Mg-Teflon exhaust plume particles. In Section 3 the model is simplified further by assuming that all the exhaust particles have the same size as well as the same average velocity. The resulting savings in computer time made it practical to investigate how the exhaust plume of a Mg-Teflon flare would look when viewed as an approximate point source by a distant IR sensor. Since the exhaust plume particles were all the same size, and this size was adjustable, it was also a straightforward matter to investigate the effect of particle size on plume radiance. Section 4 again represents the particles by a log-normal distribution, and the predictions of the model are compared to IR data acquired from three separate burning flares. These flares were part of a longer series of tests conducted in March 1988, which were designed to measure the radiance of Mg-Teflon flares burning in a vacuum. The concluding section summarizes the results of the report.

2. DERIVATION OF THE MODEL EQUATIONS

When measuring the size distribution of small irregular particles, it is customary to assume the particles are spheres and then allow for their irregularity by introducing undetermined constants into the formulas for the surface area and volume of a sphere [1]. Suppose, for example, the size distribution of a collection of microscopic cubes with sides of length λ were examined by some technique which measured directly the surface area of each particle. Not knowing that the particles were cubes, each particle would then be assigned an equivalent spherical radius R using the rule that $4\pi R^2$, the surface area of a sphere, must equal $6\lambda^2$, the surface area of a cube. It follows that $\lambda = R(2\pi/3)^{1/2}$, but the volume of that same particle, if it were truly a sphere, would be $(4/3)\pi R^3$. Since it is, in fact, a cube, its volume in reality is $\lambda^3 = (2\pi/3)^{3/2} R^3 = f_v(4/3)\pi R^3$ where $f_v = (\pi/6)^{1/2}$. It is not surprising that $f_v < 1$, because a sphere can be defined as that three-dimensional closed surface which, for a fixed amount of area, encloses the maximum possible volume. Therefore, other surfaces can be expected to enclose smaller volumes.

The exhaust particles generated by the Mg-Teflon flares described in this report have had their size distributions measured by a modified Malvern model 2600c particle sizer. The Malvern particle sizer measures the amount of light forward-scattered off microscopic particles illuminated by a helium-neon laser. From this it can estimate the fraction of particles at any given size, where the size of the particle is taken to be, in the case of spheres, the particle diameter. For a collection of irregular particles, estimates of both surface area and volume go into the Malvern calculation of the particle size distribution. Therefore, what we have done is to divide the Malvern size estimate — that is, the effective spherical diameter of a particle — by two and call the resulting number the particle scattering radius R . Then the surface area S and volume V of a particle of scattering radius R are defined to be

$$S = f_s \cdot 4\pi R^2 \quad (2.1a)$$

$$V = f_v \cdot \frac{4}{3} \pi R^3 \quad (2.1b)$$

where f_s and f_v are unknown positive constants independent of R . In effect, all the particles inside the exhaust plume have been assigned the same average irregular shape. The dimensionless constants f_s and f_v must be $O(1)$ in magnitude because the exhaust particles of the flare have been caught on glass slides, examined under a microscope, and found not to be outrageously nonspherical in shape.

In the model developed below, it is assumed that the exhaust particles of the burning flare can be described by a particle size distribution $f(R)$, where $f(R)dR$ is the probability that a particle picked at random from the flare exhaust plume has a scattering radius between R and $R + dR$. It is also assumed that $f(R)$ is a log-normal distribution

$$f(R) = \frac{1}{R\sigma\sqrt{2\pi}} e^{-\frac{[\ln(R/R_{1a})]^2}{2\sigma^2}} \quad (2.2)$$

where σ and R_{1a} are positive constants whose values will be measured by the Malvern particle sizer.

In order to predict plume radiant intensity away from the flare, it is necessary to know how the exhaust particles cool off as they travel down the plume. The particles in the exhaust plume are irregularly shaped chunks, so there is no practical way to calculate their emissivity using electromagnetic theory. It is expected, however, that when the particles are much larger than the radiation wavelength λ , their surface emissivity will approach a constant value ϵ regardless of their shape; and that when they are much smaller than the wavelength, that is, in the Rayleigh limit, their surface emissivity will be proportional to $R/\lambda = R\nu/c$, where R is the particle scattering radius, ν the radiation frequency, and c the velocity of light [2]. Therefore, it is assumed that the exhaust particles have an emissivity function \mathcal{E} which obeys the rule

$$\mathcal{E}(R\nu/c) = \begin{cases} \epsilon & \text{for } R\nu/c > 1/2\pi \\ \frac{2\pi R\epsilon\nu}{c} & \text{for } 0 \leq R\nu/c \leq 1/2\pi \end{cases} \quad (2.3)$$

The emissivity of a microscopic particle which is both chemically pure and shaped like a sphere, so that it has both a well-defined complex index of refraction n and a mathematically tractable geometry, can be predicted using electromagnetic theory (often called, in this context, Mie theory). Figures 2-1 and 2-2 graph the Mie-theory emissivity of spheres for a variety of different n values. In each case, the emissivity changes from being (more or less) constant to being proportional to R/λ at a value of $R \approx \lambda/2\pi = c/2\pi\nu$. Although the flare exhaust particles are, in general, neither chemically pure nor shaped like spheres, this behavior of the Mie-theory emissivity suggests that $R = c/2\pi\nu$ [see Equation (2.3)] is a plausible estimate of where the particle emissivity changes over from Rayleigh behavior (proportional to R/λ) to grey-body behavior (equal to a dimensionless constant ϵ).

Assuming that the flare exhaust particles are isothermal and cool off entirely by the emission of radiation, I_{tot} is defined as the amount of radiant power per unit surface area emitted by a particle of temperature T and scattering radius R . It follows from Planck's black-body radiation law and Equation (2.3) that

$$I_{\text{tot}} = \frac{2\pi R\epsilon}{c} \int_0^{c/2\pi R} \nu e_{b\nu}(T) d\nu + \epsilon \int_{c/2\pi R}^{\infty} e_{b\nu}(T) d\nu \quad (2.4)$$

where

$$e_{b\nu}(T) = \frac{2\pi h\nu^3}{c^2(e^{h\nu/kT} - 1)}$$

c = speed of light = 2.998×10^8 m/s,

h = Planck constant = 6.625×10^{-27} erg-s, and

k = Boltzmann constant = 1.380×10^{-16} erg/°K.

107853-1

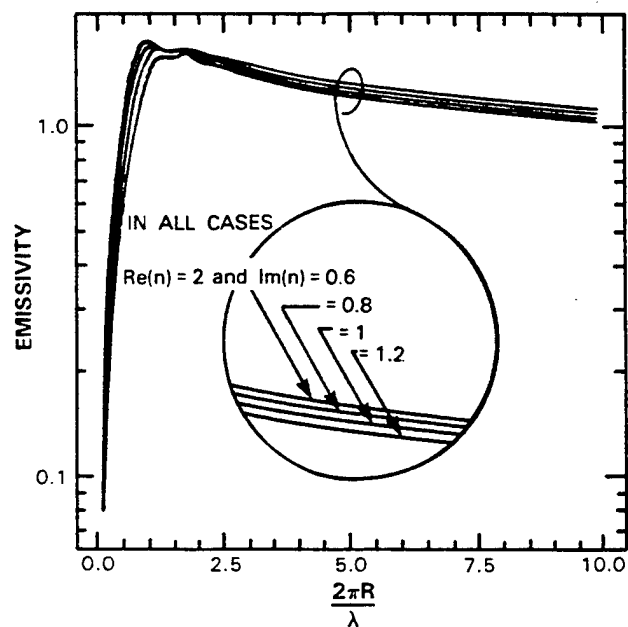


Figure 2-1 Graph of Mie-theory emissivity versus $2\pi \times (\text{particle radius}) / (\text{radiation wavelength})$ for several values of the complex index of refraction n .

107853-2

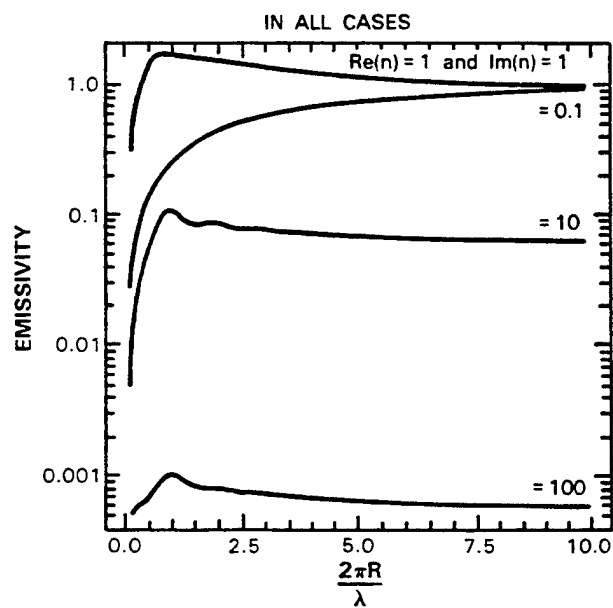


Figure 2-2 Graph of Mie-theory emissivity versus $2\pi \times (\text{particle radius}) / (\text{radiation wavelength})$ for several values of the complex index of refraction n .

The function $e_{b\nu}(T)$ is, of course, the amount of radiant power emitted from the surface of a black body at temperature T per unit surface area per unit frequency interval at frequency ν . Define a new variable $\xi = h\nu/kT$ and rewrite Equation (2.4) as

$$I_{\text{tot}} = T^5 \left(\frac{4\pi^2 R \epsilon k^4}{h^4 c^3} \right) \int_0^{hc/2\pi R k T} \xi P_\ell(\xi) d\xi + T^4 \left(\frac{2\pi \epsilon k^4}{h^3 c^2} \right) \int_{hc/2\pi R k T}^{\infty} P_\ell(\xi) d\xi \quad (2.5)$$

where

$$P_\ell(\xi) = \xi^3 / (e^\xi - 1)$$

The integrals in Equation (2.5) cannot be simplified unless $P_\ell(\xi)$ is replaced by an approximation $P_{\ell a}(\xi)$ such that

$$P_{\ell a}(\xi) = \xi^3 e^{-\xi} + \xi^2 e^{-\Omega \xi} \quad (2.6)$$

When $\Omega > 1$, both P_ℓ and $P_{\ell a}$ have the limiting form $\xi^3 e^{-\xi}$ for $\xi \rightarrow \infty$. For $x \rightarrow 0$ we have $e^x \approx 1 + x + O(x^2)$ and thus both P_ℓ and $P_{\ell a}$ have the limiting form $\xi^2 + O(\xi^3)$ when $\xi \rightarrow 0$. The value of $\Omega > 1$ in Equation (2.6) can be chosen to give the best least-squares fit of $P_{\ell a}$ to P_ℓ . When this is done, $\Omega = 1.586$, and Figure 2-3 shows that these two functions then match each other very closely indeed. Figure 2-4 shows that the maximum error involved in this approximation is several percent at most, which is quite acceptable for the purposes of this report.

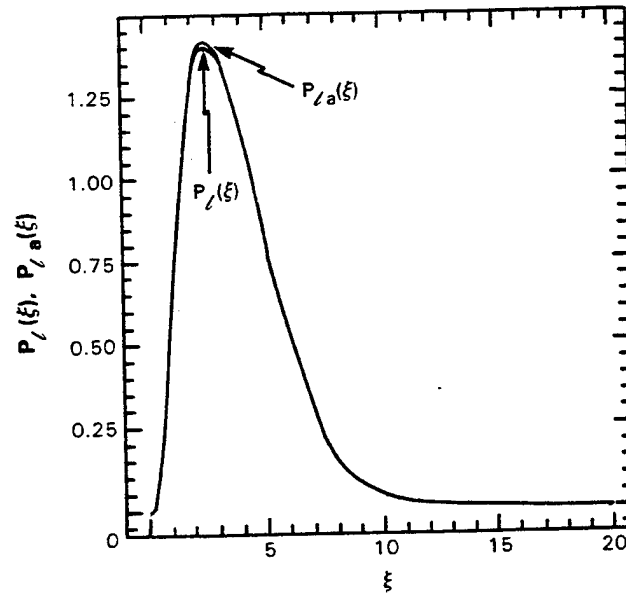


Figure 2-3. Graph of P_ℓ and its approximation $P_{\ell a}$ versus ξ .

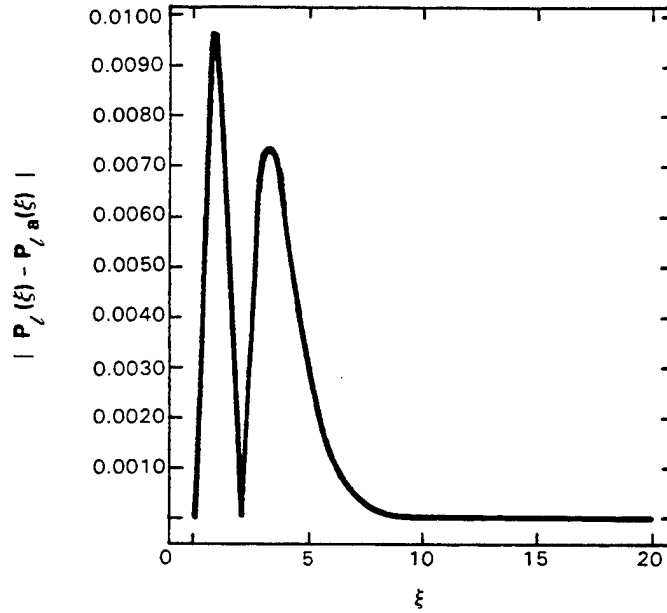


Figure 2-4. Graph of the absolute error between P_l and P_{la} versus ξ .

Replacing P_l in Equation (2.5) with P_{la} in Equation (2.6) and integrating gives

$$I_{\text{tot}} = T^4 \left(\frac{2\pi\epsilon k^4}{h^3 c^2} \right) \cdot \mathcal{J} \left(\frac{2\pi R k T}{hc} \right) \quad (2.7)$$

where

$$\begin{aligned} \mathcal{J}(x) = & 24x(1-e^{-1/x}) + 6x\Omega^{-4}(1-e^{-\Omega/x}) \\ & - e^{-1/x} (1/x^2 + 6/x + 18) \\ & - \Omega^{-2} e^{-\Omega/x} (1/x + 4/\Omega) \end{aligned}$$

with

$$\Omega = 1.586$$

An isothermal particle of density ρ and constant heat capacity C_p will lose, when its temperature drops by an amount ΔT , an amount of thermal energy ΔE given by

$$\Delta E = f_v \cdot \frac{4}{3} \pi R^3 \rho C_p \Delta T \quad (2.8)$$

where the factor f_v comes from the formula for the particle volume given in Equation (2.1b). According to Equations (2.7) and (2.1a), the particle will radiate energy at the rate of

$$\frac{dE}{dt} = -f_s \cdot 4\pi R^2 I_{\text{tot}} = -f_s R^2 T^4 \left(\frac{8\pi^2 \epsilon k^4}{h^3 c^2} \right) \cdot \mathcal{J} \left(\frac{2\pi R k T}{hc} \right) \quad (2.9)$$

Substitute Equation (2.8) into (2.9) to get

$$\frac{dT}{dt} = -\frac{6\pi A_e k^4 T^4}{R\rho C_p h^3 c^2} \cdot \mathcal{J} \left(\frac{2\pi RkT}{hc} \right) \quad (2.10)$$

where

$$A_e = \text{emissivity shape factor} = \epsilon f_s / f_v$$

Because ϵ , f_s , and f_v are all $O(1)$ quantities, it follows that A_e is also $O(1)$.

In Figure 2-5, r is defined as the distance between the flare and a particle inside its exhaust plume. Assuming that all the particles inside the exhaust plume travel (in the vacuum) at a constant velocity v_o , Equation (2.10) can be rewritten as

$$\frac{dT}{dr} = -\frac{6\pi A_e k^4 T^4}{R\rho v_o C_p h^3 c^2} \cdot \mathcal{J} \left(\frac{2\pi RkT}{hc} \right) \quad (2.11)$$

Equation (2.11) has the boundary condition

$$T|_{r=0} = T_o \quad (2.12)$$

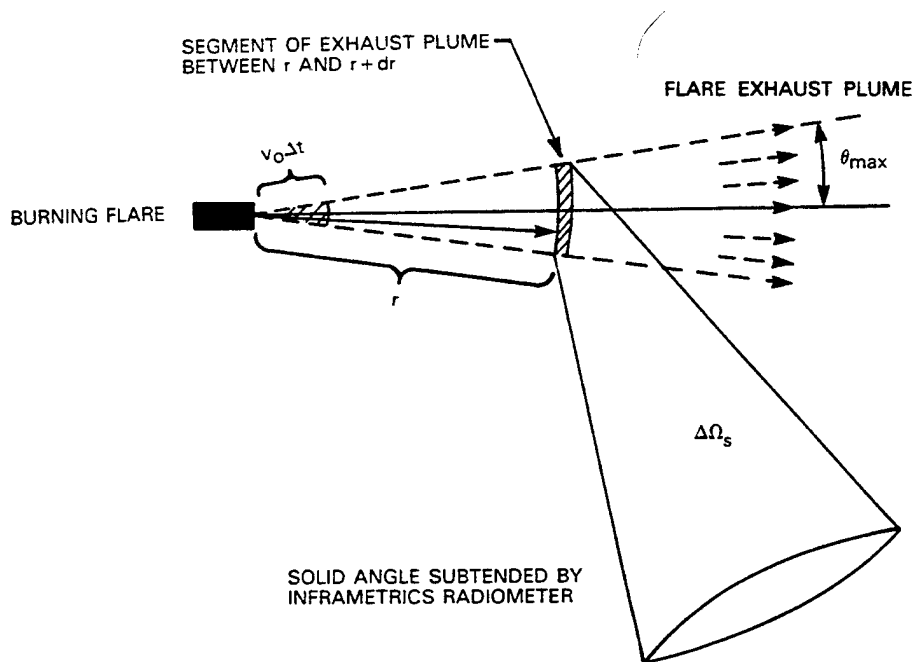


Figure 2-5 Steady-state exhaust plume generated by a flare burning in a vacuum.

where T_0 is the temperature at which all the exhaust plume particles leave the burning flare. Equations (2.11) and (2.12) taken together define a function T such that $T(r,R)$ is the temperature of an exhaust plume particle of scattering radius R located a distance r from the burning flare.

The best way to examine the behavior of function $T(r,R)$ is to nondimensionalize Equations (2.11) and (2.12).

$$\frac{dx}{dq} = -x^4 \mathcal{T}(x) \quad (2.13a)$$

where

$$x = \left(\frac{2\pi Rk}{hc} \right) T \quad , \quad (2.13b)$$

$$q = \left(\frac{3A_e ck}{4\pi^2 R^4 \rho v_o C_p} \right) r \quad , \quad \text{and} \quad (2.13c)$$

$$x|_{q=0} = x_0 = \frac{2\pi RkT_0}{hc} \quad . \quad (2.13d)$$

Figures 2-6 and 2-7 give x as a function of q for two different ranges of x_0 values.

The steady-state combustion rate of a burning flare can be represented by a constant P such that $P\Delta t$ is the amount of mass burned by the flare in time Δt . Figure 2-5 shows that the mass of all the exhaust particles emitted by the flare in time Δt must lie within a distance $v_o \Delta t$ of the flare's burning surface. Hence,

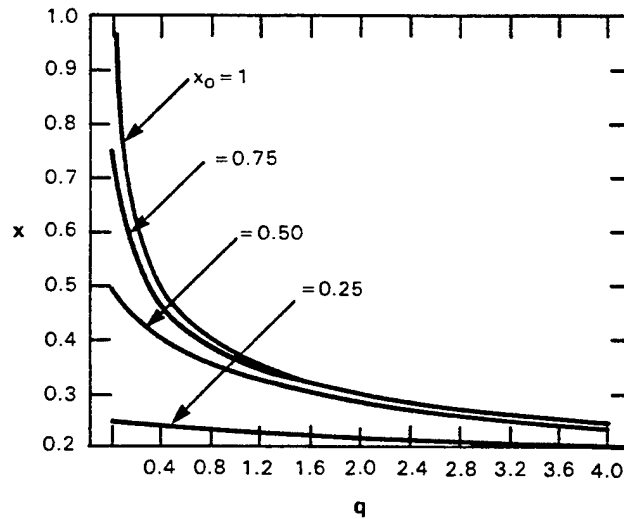


Figure 2-6 Graph of x versus q for $x_0 = 0.25, 0.50, 0.75, 1$.

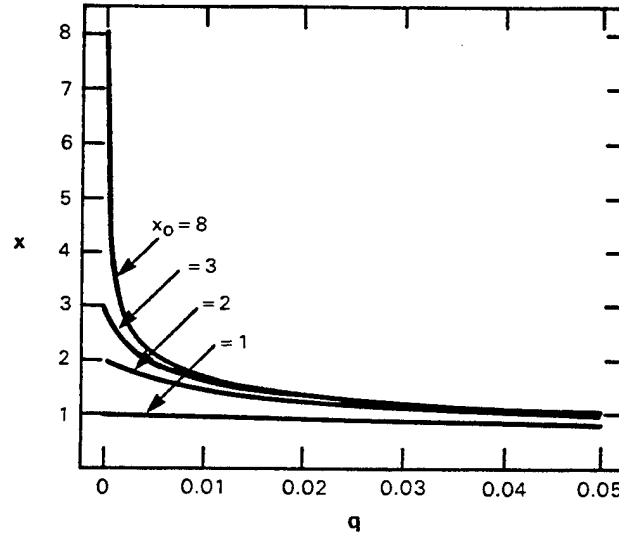


Figure 2-7 Graph of x versus q for $x_0 = 1, 2, 3, 8$.

$$P\Delta t = (\Lambda_p v_o \Delta t) \cdot \int_0^\infty f_v \cdot \left(\frac{4}{3} \pi R^3 \rho \right) f(R) dR \quad (2.14)$$

where Λ_p is a positive constant such that $\Lambda_p dr$ is the number of particles located between r and $r + dr$ inside the flare exhaust plume, ρ is the average density of the exhaust plume particles [see Equation (2.8)], f_v has been defined in Equation (2.1b), and $f(R)$ has been defined in Equation (2.2).

Equation (2.14) can be rearranged to give

$$\Lambda_p = \frac{3P}{4\pi\rho f_v v_o} \left[\int_0^\infty R^3 f(R) dR \right]^{-1} = \frac{3Pe^{-9\sigma^2/2}}{4\pi\rho f_v v_o R_{la}^3} \quad (2.15)$$

where in the second step of Equation (2.15) we have substituted from Equation (2.2) to get

$$\int_0^\infty R^3 f(R) dR = R_{la}^3 e^{9\sigma^2/2} \quad (2.16)$$

A radiometric measurement is used (see Figure 2-5) to capture the radiation emitted by all the exhaust plume particles located between r and $r + dr$ inside the exhaust plume of the burning flare. Although a single particle will have a distinct irregular shape and thus cannot emit radiation isotropically, it is safe to assume that a large collection of such particles will, being randomly aligned with respect to the radiometer, emit their collective radiation isotropically. Thus,

on the average, the amount of radiant power per unit wavelength at wavelength λ emitted by a single particle of scattering radius R and temperature T into the solid angle $\Delta\Omega_s$ subtended by the Inframetrics radiometer is

$$\frac{\Delta\Omega_s}{4\pi} \cdot (f_s 4\pi R^2) \cdot \mathcal{E}(R/\lambda) \cdot e_{b\lambda}(T)$$

where

$$e_{b\lambda}(T) = \frac{C_1}{\lambda^5 (e^{C_2/\lambda T} - 1)},$$

$$C_1 = 3.74 \times 10^{-16} \text{ w-m}^2, \quad \text{and}$$

$$C_2 = 1.44 \times 10^{-2} \text{ m-}^\circ\text{K}.$$

Function \mathcal{E} is defined in Equation (2.3) and f_s is defined in Equation (2.1a). Function $e_{b\lambda}(T)$ is the amount of radiant power emitted from the surface of a black body at temperature T per unit surface area per unit wavelength interval at wavelength λ . Call $G(\lambda, r) dr d\lambda d\Omega$ the amount of radiant power emitted by all particles located between r and $r + dr$ at wavelengths between λ and $\lambda + d\lambda$ into a solid angle $d\Omega$. If the exhaust plume is optically thin* so that the particles do not absorb or scatter significant amounts of radiation, it follows that

$$G(\lambda, r) = f_s \cdot \Lambda_p \cdot \int_0^\infty dR R^2 f(R) e_{b\lambda}(T(r, R)) \cdot \mathcal{E}(R/\lambda)$$

$$= \frac{3A_e P C_1 e^{-9\sigma^2/2}}{4\pi \rho v_o R_{la}^3 \lambda^5} \int_0^\infty dR R^2 \frac{f(R) \mathcal{M}(R/\lambda)}{e^{C_2/\lambda T(r, R)} - 1} \quad (2.17)$$

where in the second step of Equation (2.17) we have substituted the expression for Λ_p in Equation (2.15) and A_e in Equation (2.10). We have also taken the constant ϵ outside the integral by defining that

$$\mathcal{M}(x) = \frac{1}{\epsilon} \mathcal{E}(x) = \begin{cases} 1 & \text{for } x > 1/2\pi \\ 2\pi x & \text{for } 0 \leq x \leq 1/2\pi \end{cases} \quad (2.18)$$

Equations (2.2), (2.11), (2.12), (2.17), and (2.18) define the model used to predict the radiant intensities of exhaust plumes generated by Mg-Teflon flares burning in a vacuum.

* A TV camera was mounted inside the space chamber to watch both the flare and its associated exhaust plume. The burning surface of the flare could easily be seen even when viewed through the central portions of the plume, showing the plume to be optically thin to visible light. IR radiation, having a longer wavelength, should be attenuated even less.

3. INVESTIGATION OF AN EXOATMOSPHERIC FLARE

It is instructive to simplify the exhaust plume model by taking the limit as $\sigma \rightarrow 0$ in Equation (2.2), transforming $f(R)$ into the dirac-delta function $\delta(R-R_{la})$. This gives all the exhaust plume particles the same scattering radius $R_o = R_{la}$ and allows investigation (without using an excessive amount of computer time) of how the exhaust plume of a vacuum-burning Mg-Teflon flare looks when viewed as an approximate point source by a distant IR sensor.

Assume that the particle concentration $C(r, \theta)$ (with units of particles per unit volume) at a given point inside the exhaust plume is a function of both r and θ , the spherical polar coordinates of that point as defined in Figure 3-1. Say that

$$C(r, \theta) \begin{cases} \Psi/r^2 & \text{for } 0 \leq \theta \leq \theta_{\max} \\ 0 & \text{for } \theta > \theta_{\max} \end{cases} \quad (3.1)$$

where Ψ is a constant having units of inverse length. The constant Δ_p has already been defined by the requirement that $\Delta_p dr$ be the number of particles located between r and $r + dr$ inside the flare exhaust plume [see Equation (2.14) et. seq.]. Test whether Equation (3.1) has left Δ_p a constant by writing

$$\Delta_p dr = r^2 dr \int_0^{2\pi} d\theta \int_0^{\theta_{\max}} d\theta \sin \theta C(r, \theta) \quad (3.2)$$

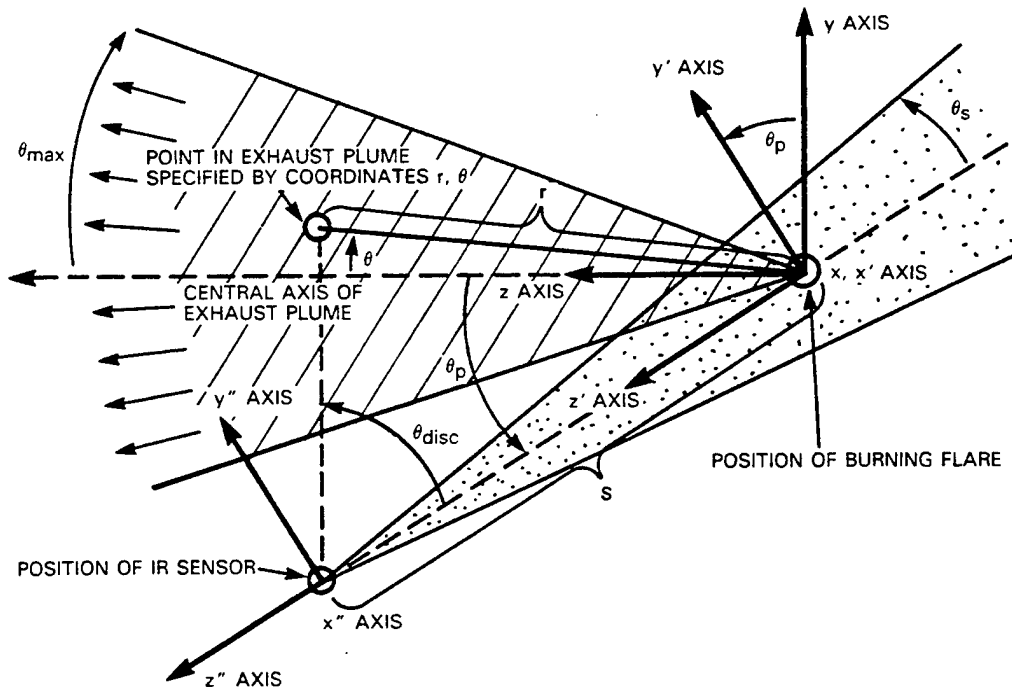


Figure 3-1. Three coordinate systems used to investigate how a Mg-Teflon exhaust plume would look when viewed by a distant IR sensor.

Substitute Equation (3.1) into (3.2) and get

$$\Delta_p = \Psi \Delta \Omega \quad (3.3)$$

where

$$\Delta \Omega = \text{solid angle subtended by the exhaust plume cross section} \\ + 2\pi(1 - \cos\theta_{\max})$$

Substitute Equation (3.3) into (2.15), take the limit as $\sigma \rightarrow 0$, and replace R_{la} by R_o to get

$$\Psi = \Delta_p / \Delta \Omega = \frac{3P}{4\pi\rho f_v v_o R_o^3 \Delta \Omega} \quad (3.4)$$

Equations (3.3) and (3.4) demonstrate that Δ_p is indeed still a constant, so Equations (2.17) and (2.18) still hold. Take the limit of Equation (2.17) as $\sigma \rightarrow 0$ and set $R_{la} = R_o$ to get

$$G_o(\lambda, r) = \frac{3A_e P \mathcal{M}(R_o/\lambda)}{4\pi\rho v_o R_o \lambda^5} \left(\frac{C_1}{e^{C_2/\lambda T(r, R_o)} - 1} \right) \quad (3.5)$$

The subscript "o" has been added to G as an indication that Equation (3.5) should only be used when all exhaust plume particles have the same scattering radius R_o .

Since the particles traveling down the flare exhaust plume will never cool down to absolute zero in a finite amount of time, the exhaust plume can, in principle, be regarded as infinitely long. To treat the plume as an approximate point source when viewed by a distant IR sensor, we must give the plume some finite length. This is done by picking a temperature $T_f < T_o$, where T_o is the temperature at which the particles leave the burning flare, such that all particles with temperatures $T \leq T_f$ are assumed to contribute only negligible amounts of radiation to the total output of the exhaust plume. (In the work done below $T_f = 200^\circ\text{K}$.) The length of the exhaust plume corresponding to T_f is called L_f where from Equation (2.11)

$$L_f = \frac{\rho R_o v_o C_p h^3 c^2}{6\pi A_e k^4} \int_{T_f}^{T_o} \frac{dT}{T^4 \mathcal{J}(2\pi R_o k T / hc)} \quad (3.6)$$

with $R = R_o$ because now all the exhaust plume particles have the same scattering radius. In fact, L_f is the maximum value of the radius coordinate r , and for any temperature value T between T_f and T_o we can associate a unique radius value r such that

$$r(T) = \frac{\rho R_o v_o C_p h^3 c^2}{6\pi A_e k^4} \int_T^{T_o} \frac{dT'}{T'^4 \mathcal{J}(2\pi R_o k T' / hc)} \quad (3.7)$$

Approximate \mathcal{J} in Equation (3.7) by the function

$$\mathcal{J}_a(x) = \frac{x + \underline{w}x^3}{\underline{u} + v(x + \underline{w}x^3)} \quad (3.8)$$

The values of u and v come from the requirement that

$$\left. \frac{\mathcal{J}(x)}{x} \right|_{x \ll 1} \cong 24 + \frac{6}{\Omega^4} \cong 24.95,$$

so

$$u = (24.95)^{-1} = 0.04008;$$

and

$$\left. \mathcal{J}(x) \right|_{x \gg 1} \cong 6 + \frac{2}{\Omega^3} \cong 6.501,$$

so

$$v = (6.501)^{-1} = 0.1538.$$

For the values of R_0 and T typical of vacuum-burning Mg-Teflon flares, it is known that $x = 2\pi R_0 kT/hc$, the argument of \mathcal{J} , lies somewhere between 0.005 and 10. Therefore, in Equation (3.8) \underline{w} is adjusted to give the best least-squares fit of \mathcal{J}_a to \mathcal{J} for $0.005 \leq x \leq 10$, and $\underline{w} = 44.02$. Figure 3-2 demonstrates how closely \mathcal{J}_a matches \mathcal{J} for x values between 0.005 and 10, and Figure 3-3 graphs the absolute error between \mathcal{J}_a and \mathcal{J} as a function of x . The maximum error never exceeds 10 percent, which is adequate for our purposes.

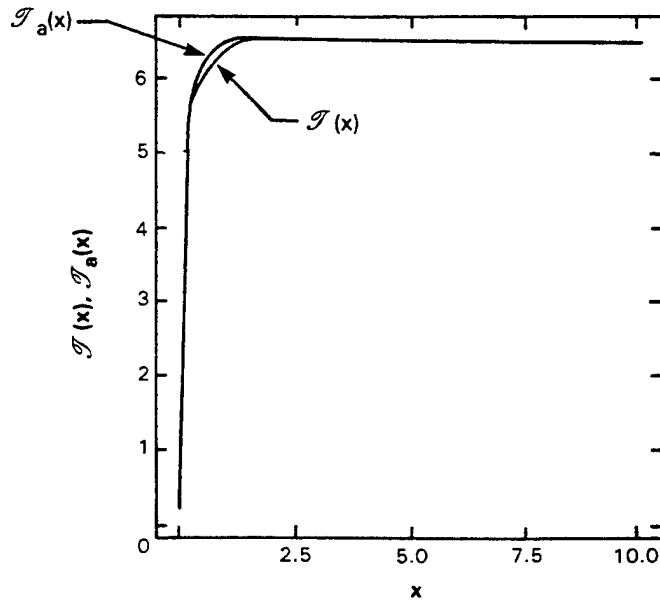


Figure 3-2 Graph of \mathcal{J} and its approximation \mathcal{J}_a versus x .

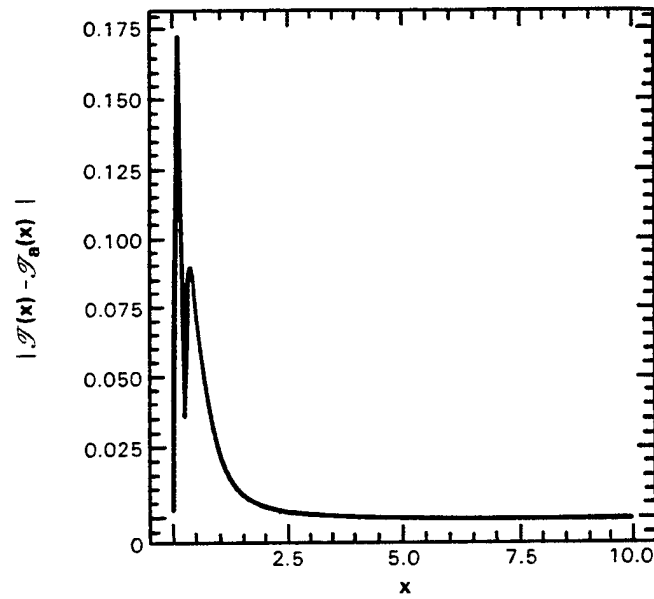


Figure 3-3 Graph of the absolute error between \mathcal{J} and \mathcal{J}_a versus x .

Substitute Equation (3.8) into (3.7) to get

$$r(T) \equiv r_a(T) = \frac{\rho R_o^4 v_o C_p h^3 c^2}{6\pi A_e k^4} \int_{R_o T}^{R_o T_o} \frac{d\zeta}{\zeta^5} \left(\frac{u + v\zeta + w\zeta^3}{1 + w\zeta^2} \right) \quad (3.9)$$

where

$$\begin{aligned} \zeta &= R_o T, \\ u &= 9.181 \times 10^{-3} \text{ cm}^\circ\text{K}, = \underline{u}(hc/k) \\ v &= 0.1538 \text{ (dimensionless), and} \\ w &= 838.9 \text{ (cm}^\circ\text{K)}^{-2} = \underline{w}(k/hc)^2. \end{aligned}$$

Equation (3.9) can be simplified using partial fractions.

$$\begin{aligned} r_a(T) &= \frac{\rho R_o^4 v_o C_p h^3 c^2}{6\pi A_e k^4} \int_{R_o T}^{R_o T_o} d\zeta \left(\frac{uw^2}{\zeta} - \frac{uw}{\zeta^3} + \frac{v}{\zeta^4} + \frac{u}{\zeta^5} - \frac{uw^3\zeta}{1 + w\zeta^2} \right) \\ &= \frac{\rho R_o^4 v_o C_p h^3 c^2}{6\pi A_e k^4} \left\{ uw^2 \left(\frac{T_o}{T} \sqrt{\frac{1 + w R_o^2 T^2}{1 + w R_o^2 T_o^2}} \right) - \frac{uw}{2R_o^2} \left(\frac{1}{T^2} - \frac{1}{T_o^2} \right) \right. \\ &\quad \left. + \frac{v}{3R_o^3} \left(\frac{1}{T^3} - \frac{1}{T_o^3} \right) + \frac{u}{4R_o^4} \left(\frac{1}{T^4} - \frac{1}{T_o^4} \right) \right\}. \end{aligned} \quad (3.10)$$

Equation (3.10) is, computationally, a much quicker formula for $r(T)$ than is Equation (3.7), and that is why function \mathcal{T}_a has been used to approximate \mathcal{T} .

To calculate the response of the IR sensor to the radiating exhaust plume of the flare, simply add the radiation emitted by all particles seen at a temperature T for all temperatures T between T_o and T_f . To do this correctly, it must be known how many particles at any given temperature T lie within the sensor field of view (FOV). From Equation (3.7) it is known that all the particles at a given temperature T lie on a sphere of radius $r(T)$ surrounding the flare. From Equation (3.1), it is known that these exhaust particles will be evenly distributed over a spherical cap created, as shown in Figure 3-4, by the intersection of the conical exhaust plume of the flare with a sphere of radius $r(T)$. Assume the sensor FOV is a cone of half angle θ_s with the burning flare on the cone central axis a distance s away from the sensor (see Figure 3-1). The observation angle θ_p is defined as the angle between the central axis of the flare exhaust plume and the central axis of the sensor FOV. When θ_p is 90° , the sensor observes the exhaust plume broadside; when $\theta_p < \theta_{max}$, the sensor is located "inside" the flare exhaust plume.

Function $A(r/s, \theta_p, \theta_s, \theta_{max})$ is defined as the fraction of the total area of the spherical cap shown in Figure 3-4 (located on the surface of a sphere of radius r) which lies inside the conical sensor FOV shown in Figure 3-1 (located a distance s away from the burning flare). Obviously, A must depend on θ_p , θ_s , and θ_{max} , but it may not be clear at first why A depends only on the ratio of r/s rather than on r and s as separate variables. Note that by definition, A is a dimensionless fraction which always satisfies the inequality $0 \leq A \leq 1$. Consequently, distance can be measured in any convenient unit and there is no reason not to choose s , the distance between the flare and the sensor, as our unit of length. Thus, we can define a new dimensionless length $u = r/s$ and know, because A , θ_p , θ_s , and θ_{max} are also dimensionless, that A can only depend on u , θ_p , θ_s , and θ_{max} .

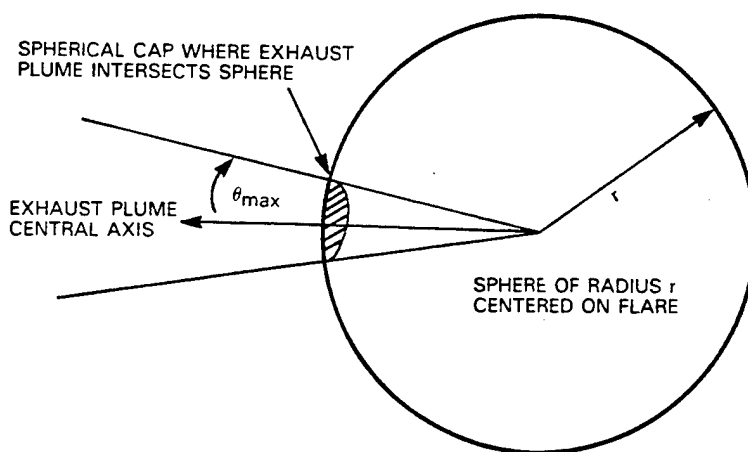


Figure 3-4. How a conical exhaust plume intersects an imaginary sphere centered on the burning flare.

Function A was calculated numerically using a Monte Carlo computer program which generated N random points evenly distributed over a spherical cap a distance u away from the burning flare. (The size of the spherical cap, of course, depends on both u and θ_{\max} .) For each of these points, the computer program calculated an angle θ_{disc} (see Figure 3-1) and checked whether or not that point lay within the sensor FOV (that is, whether $\theta_{\text{disc}} \leq \theta_s$). By counting the number of points having $\theta_{\text{disc}} \leq \theta_s$ and dividing by N, the program obtains an estimate for A. The larger the value of N, the more accurate that estimate. For the results given in this report, $N \geq 10^4$.

A double coordinate transformation was used to derive the formula for θ_{disc} . The central axis of the exhaust plume is taken to be the z axis of the unprimed Cartesian coordinate system shown in Figure 3-1. The y axis of that coordinate system points up, and the x axis points out of the page. A single-primed coordinate system is defined by rotating the unprimed system through an angle θ_p about its x axis [see Figures 3-1 and 3-5(a)]. Now the z' axis points toward the sensor. The second coordinate transformation creates a double-primed coordinate system and is a translation along the z' axis by a distance s [Figure 3-5(b)]; then the origin of the double-primed coordinate system coincides with the position of the sensor and the negative z'' axis lies along the central axis of the sensor FOV. If x,y,z are the unprimed coordinates of some point lying on the spherical cap, and x'',y'',z'' are the coordinates of the same point in the double-primed coordinate system, then

$$\begin{aligned} x'' &= x, \\ y'' &= y \cos \theta_p + z \sin \theta_p, \text{ and} \\ z'' &= -s - y \sin \theta_p + z \cos \theta_p \end{aligned} \quad (3.11)$$

We can also represent the position of that point using spherical coordinates r, θ , ϕ in the unprimed coordinate system

$$\begin{aligned} x &= r \sin \theta \cos \phi \\ y &= r \sin \theta \sin \phi \\ z &= r \cos \theta \end{aligned} \quad (3.12)$$

Similarly, use spherical coordinates r'', θ'' , ϕ'' to represent the position of the point in the double-primed coordinate system. From Figure 2-2, angle θ'' is

$$\theta'' = \pi - \theta_{\text{disc}} = \tan^{-1} \left(\frac{\sqrt{(x'')^2 + (y'')^2}}{z''} \right) \quad (3.13)$$

Hence, substitute Equations (3.12) into (3.11), substitute the resulting equations into (3.13), and then set $\theta_{\text{disc}} = \pi - \theta''$. This gives a formula for θ_{disc} in terms of θ_p (the observation angle), angles θ and ϕ (the spherical angles in the unprimed coordinate system), and u (the dimensionless distance of the spherical cap from the burning flare).

$$\theta_{\text{disc}} = \tan^{-1} \left(\frac{u \sqrt{b}}{1 + au} \right) \quad (3.14)$$

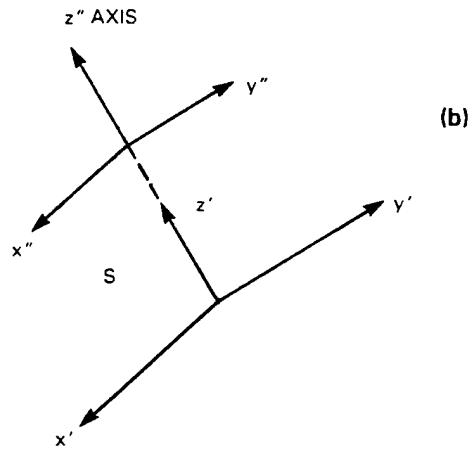
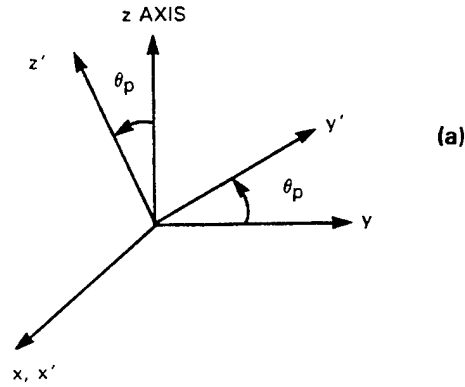


Figure 3-5. Transformation from the (a) unprimed to the primed coordinate system; and (b) primed to the double-primed coordinate system.

where

$$a = \sin\theta \sin\phi \sin\theta_p - \cos\theta \cos\theta_p, \text{ and}$$

$$b = \sin^2\theta \cos^2\phi + (\sin\theta \sin\phi \cos\theta_p + \cos\theta \sin\theta_p)^2$$

When the Monte Carlo program generates a random point, in reality it chooses a pair of random θ, ϕ values using the formula

$$\theta = \sin^{-1} \left\{ \sqrt{1 - [1 + Q(\cos\theta_{\max} - 1)]^2} \right\} \quad (3.15)$$

$$\phi = 2\pi Q$$

If Q is uniformly distributed between 0 and 1, then angles θ and ϕ will be uniformly distributed over the unit sphere with $0 \leq \theta \leq \theta_{\max}$ and $0 \leq \phi \leq 2\pi$. Having generated a pair of random θ, ϕ values, the program calculates θ_{disc} from the formula shown in Equation (3.14) and decides whether or not the pair of θ, ϕ values lie within the sensor FOV. Figures 3-6, 3-7, and 3-8 are graphs of A versus u for $\theta_s = 0.1^\circ$; $\theta_{\max} = 15^\circ, 30^\circ, 45^\circ$; and $\theta_p = 0^\circ, 30^\circ, 60^\circ, 90^\circ$.

In Figure 3-6, the curves representing A for $\theta_p = 30^\circ, 60^\circ$, and 90° all drop to zero at finite values of u , but the value for $\theta_p = 0^\circ$ only approaches zero asymptotically. This is understood by noting that for $\theta_p = 0^\circ$ the sensor is always inside the plume and will have parts of the plume within its FOV for all values of $u < 1$. In Figure 3-7, both the curves for $\theta_p = 0^\circ$ and for $\theta_p = 30^\circ$ approach zero asymptotically, and the curve for $\theta_p = 30^\circ$ is always less than the curve for $\theta_p = 0^\circ$. Again this makes sense, because $\theta_p = \theta_{\max} = 30^\circ$, so the $\theta_p = 30^\circ$ curve lies on one edge of the plume as $u \rightarrow 1$. Thus, it will never reach zero and yet always be smaller than the $\theta_p = 0^\circ$ curve, which lies entirely inside the plume. In Figure 3-8, for values of u greater than 0.006 and less than 1, the $\theta_p = 30^\circ$ and $\theta_p = 0^\circ$ curves become identical (allowing for the randomness of the Monte Carlo estimate). In this case, $\theta_p < \theta_{\max}$ for both $\theta_p = 0^\circ$ and $\theta_p = 30^\circ$, so as $u \rightarrow 1$ eventually both sensor locations will lie entirely inside the plume and have the same A values.

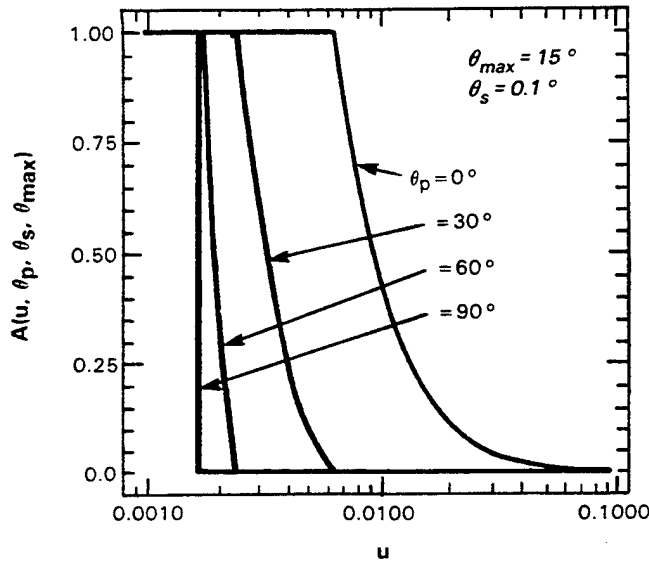


Figure 3-6. Graph of A versus u for $\theta_{\max} = 15^\circ$, $\theta_s = 0.1^\circ$, and $\theta_p = 0^\circ, 30^\circ, 60^\circ, 90^\circ$.

We define J_λ to be the radiant energy per unit time per unit wavelength interval at wavelength λ per unit solid angle emitted by plume particles located between $r = 0$ and $r = L_f$. From Equation (3.5) and the definition of A it follows that

$$J_\lambda = \int_0^{L_f} G_o(\lambda, r) A(r/s, \theta_p, \theta_s, \theta_{\max}) dr = \frac{3A_e PC_1 \mathcal{M}(R_o/\lambda)}{4\pi \rho v_o R_o \lambda^5} \int_0^{L_f} dr \frac{A(r/s, \theta_p, \theta_s, \theta_{\max})}{e^{C_2/\lambda T(r, R_o)} - 1} \quad (3.16)$$

107853-13

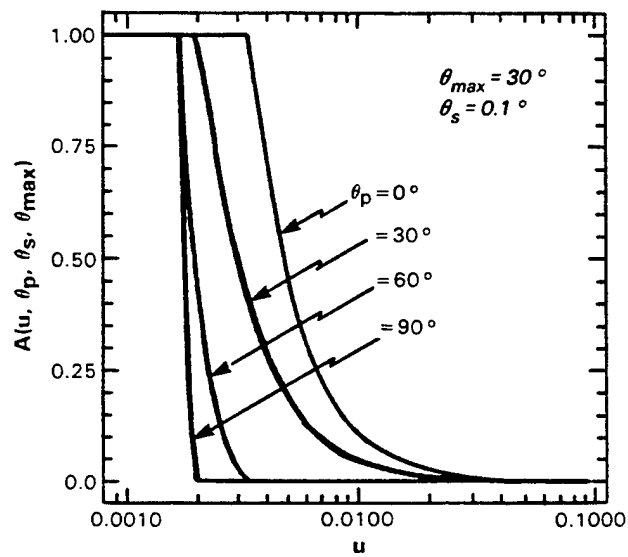


Figure 3-7. Graph of A versus u for $\theta_{\max} = 30^\circ$, $\theta_s = 0.1^\circ$ and $\theta_p = 0^\circ, 30^\circ, 60^\circ, 90^\circ$.

107853-14

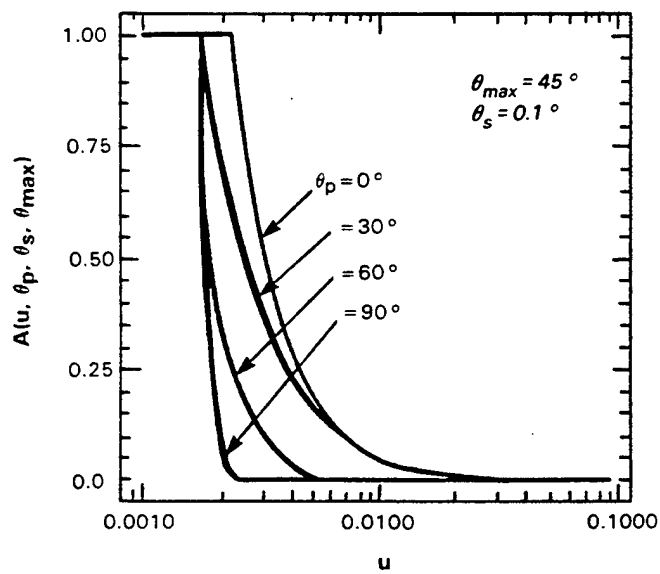


Figure 3-8. Graph of A versus u for $\theta_{\max} = 45^\circ$, $\theta_s = 0.1^\circ$ and $\theta_p = 0^\circ, 30^\circ, 60^\circ, 90^\circ$.

Because A has been evaluated numerically, J_λ must also be evaluated numerically in Equation (3.16). It is helpful to write this equation as

$$\frac{J_\lambda}{P} \cong \frac{3C_1 \mathcal{M}(R_0/\lambda)}{4\pi\rho(v_0/A_e)R_0\lambda^5} \int_{T_f}^{T_0} dT \frac{A(r_a(T)/s, \theta_p, \theta_s, \theta_{\max})}{|dT/dr|(e^{C_2/\lambda T} - 1)} \quad (3.17)$$

where the variable of integration has been changed from r to T and we have used $r_a(T)$ to approximate $r(T)$. The formula for $|dT/dr|$ comes from Equation (2.11).

Equation (3.17) is used to calculate the data shown in Figures 3-9 through 3-16. In these calculations, T_0 and T_f are always set equal to 1500°K and 200°K , respectively. Carbon and magnesium difluoride are the two basic products of Mg-Teflon combustion, so ρ has been set equal to the average of the mass densities of bulk carbon and magnesium difluoride (2.6 gm/cm^3). The value of the heat capacity C_p was set to $1.0 \times 10^7 \text{ ergs/gm/}^\circ\text{K}$, because both carbon (whose C_p values vary with temperature) and magnesium difluoride have heat capacities of this order of magnitude for temperatures between 200° and 1500°K .

Figures 3-9 and 3-10 are graphs of J_λ/P for $s = 100 \text{ km}$; $\theta_{\max} = 30^\circ$; $\theta_s = 0.1^\circ$; and $\theta_p = 0^\circ, 30^\circ, 60^\circ$, and 90° . [The "kink" in the graph of Figure 3-9 comes from the discontinuous slope of function \mathcal{M} defined in Equation (2.18).] The ratio v_0/A_e is 300 m/s (remember that A_e is dimensionless) in both Figures 3-9 and 3-10; their only difference is that $R_0 = 1 \mu\text{m}$ in Figure 3-9 while $R_0 = 10 \mu\text{m}$ in Figure 3-10. Keeping in mind that $\theta_p = 90^\circ$ is always a broadside view of the exhaust plume, it can be seen that in each case the amount of radiant energy J_λ emitted at relatively long wavelengths ($\lambda \geq 5 \mu\text{m}$) increases as θ_p decreases to zero. This is a purely geometric

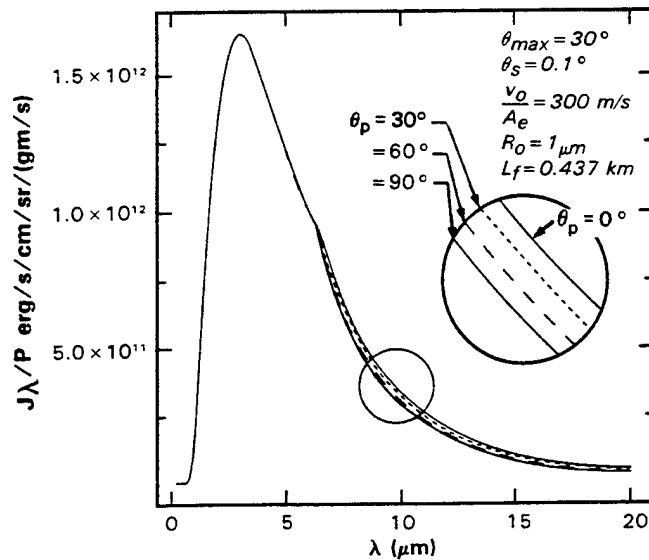


Figure 3-9 Graph of J_λ/P versus λ for $s = 100 \text{ km}$, $\theta_{\max} = 30^\circ$, $\theta_s = 0.1^\circ$, $v_0/A_e = 300 \text{ m/s}$, $R_0 = 1 \mu\text{m}$, and $L_f = 0.437 \text{ km}$.

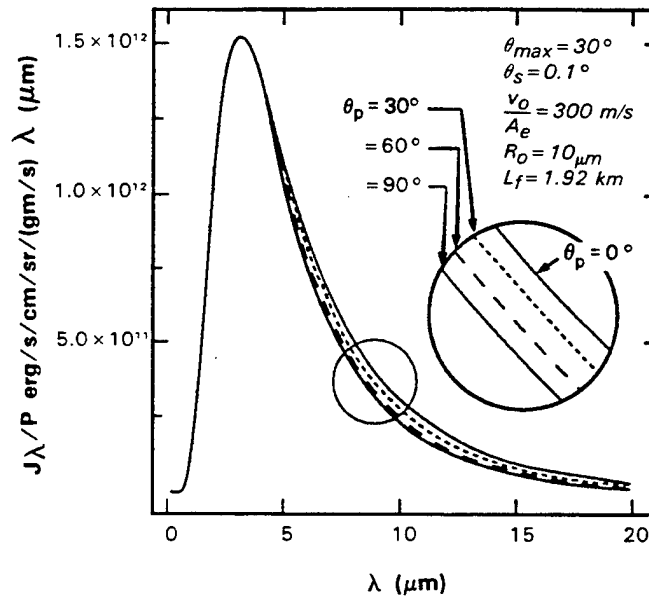


Figure 3-10 Graph of J_λ/P versus λ for $s = 100$ km, $\theta_{\max} = 30^\circ$, $\theta_s = 0.1^\circ$, $v_o/A_e = 300$ m/s, $R_o = 10$ μm , and $L_f = 1.92$ km.

phenomenon: as θ_p gets smaller, the sensor will see more exhaust particles at greater distances from the flare; being somewhat cooler (but not cold), these particles will present the sensor with more energy at longer wavelengths. Comparing Figures 3-9 and 3-10, it can be seen that this phenomenon grows more pronounced as the particle radius R_o increases. This effect can also be understood geometrically. A large particle cools more slowly than a small one, thus making the flare exhaust plume longer and bringing more cool particles into the sensor FOV at observation angles $\theta_p < 90^\circ$. Another way of looking at this is to note that if all the particles cooled off rapidly in the immediate vicinity of the burning flare, the plume would be so short it would behave like a perfect point source, making the J_λ/P curve look the same for all values of θ_p .

Perhaps the best way to analyze the increase of J_λ/P at long wavelengths is to construct the function

$$E_\lambda \Big|_{\theta_p = \theta_p} = \left(J_\lambda \Big|_{\theta_p = \theta_p} - J_\lambda \Big|_{\theta_p = 90^\circ} \right) / \left(J_\lambda \Big|_{\theta_p = 90^\circ} \right) \quad (3.18)$$

Clearly, E_λ is just the fractional increase of J_λ at an observation angle $\theta_p < 90^\circ$ compared to J_λ at an observation angle $\theta_p = 90^\circ$ (that is, viewed broadside). Figures 3-11 through 3-16 graph E_λ versus λ for $\theta_p = 0^\circ$, 30° , and 60° ; in each case E_λ behaves as expected by decreasing as θ_p increases. In all these graphs $s = 100$ km, $\theta_s = 0.1^\circ$, and $R_o = 10$ μm .

In Figures 3-11 through 3-13, $v_o/A_e = 100$ m/s and in 3-14 through 3-16, $v_o/A_e = 300$ m/s. Angle θ_{\max} is 15° in Figures 3-11 and 3-14, 30° in Figures 3-12 and 3-15, and 45° in Figures 3-13 and 3-16. An examination of Figures 3-11, 3-12, and 3-13 shows that as θ_{\max} increases, E_λ

decreases. The easiest way to understand this is to realize that larger values of θ_{\max} mean that the flare exhaust plume fills up greater portions of the spherical volume surrounding the flare. This gives the plume a greater tendency to spherical symmetry, which leads to a lesser dependence of J_λ on θ_p . The same effect is seen in Figures 3-14, 3-15, and 3-16. Another point worth mentioning, after comparing Figures 3-11, 3-12, and 3-13 to Figures 3-14, 3-15, and 3-16, is that as v_o/A_e increases, so does E_λ . Larger values of v_o/A_e cause L_f , the exhaust plume length, to increase, and this implies a greater geometric radiance effect on J_λ at observation angles $\theta_p < 90^\circ$. Thus, increasing the value of v_o/A_e has the same effect as increasing the value of R_o in Figures 3-9 and 3-10; the further the particles travel before cooling to a given temperature, the greater the dependence of J_λ on θ_p at long wavelengths.

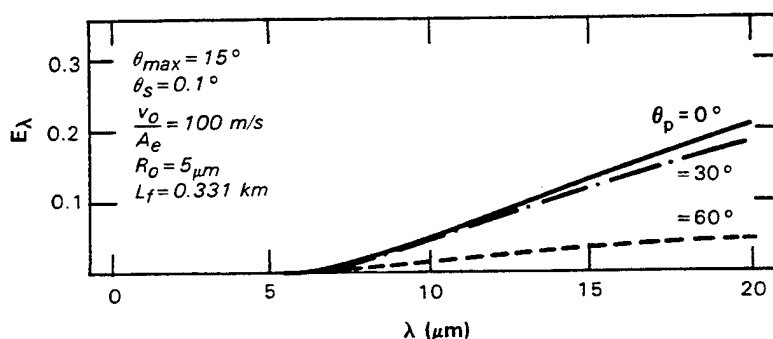


Figure 3-11 Graph of E_λ versus λ for $s = 100 \text{ km}$, $\theta_{\max} = 15^\circ$, $\theta_s = 0.1^\circ$, $v_o/A_e = 100 \text{ m/s}$, $R_o = 5 \mu\text{m}$, and $L_f = 0.331 \text{ km}$.

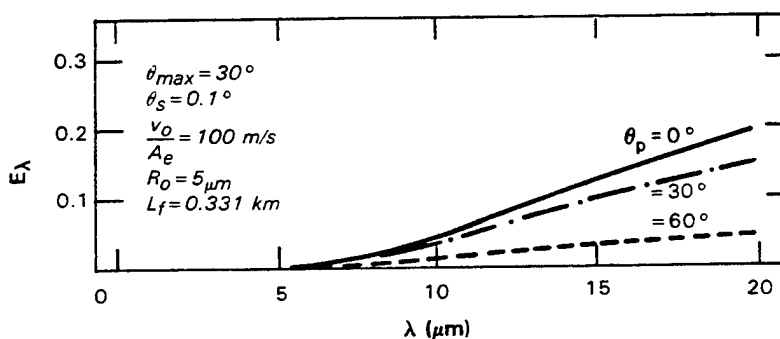


Figure 3-12 Graph of E_λ versus λ for $s = 100 \text{ km}$, $\theta_{\max} = 30^\circ$, $\theta_s = 0.1^\circ$, $v_o/A_e = 100 \text{ m/s}$, $R_o = 5 \mu\text{m}$, and $L_f = 0.331 \text{ km}$.

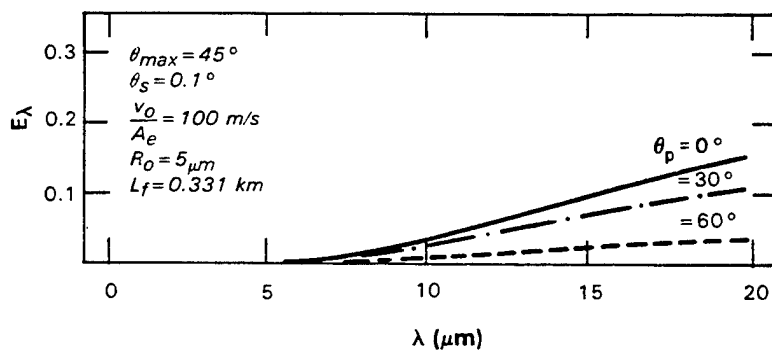


Figure 3-13 Graph of E_λ versus λ for $s = 100 \text{ km}$, $\theta_{max} = 45^\circ$, $\theta_s = 0.1^\circ$, $v_o/A_e = 100 \text{ m/s}$, $R_o = 5 \mu\text{m}$, and $L_f = 0.331 \text{ km}$.

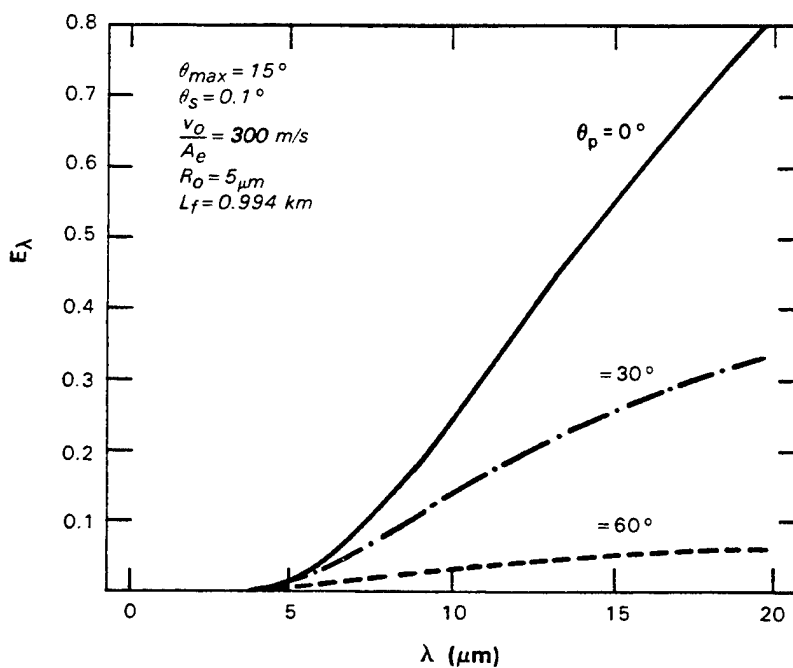


Figure 3-14 Graph of E_λ versus λ for $s = 100 \text{ km}$, $\theta_{max} = 15^\circ$, $\theta_s = 0.1^\circ$, $v_o/A_e = 300 \text{ m/s}$, $R_o = 5 \mu\text{m}$, and $L_f = 0.994 \text{ km}$.

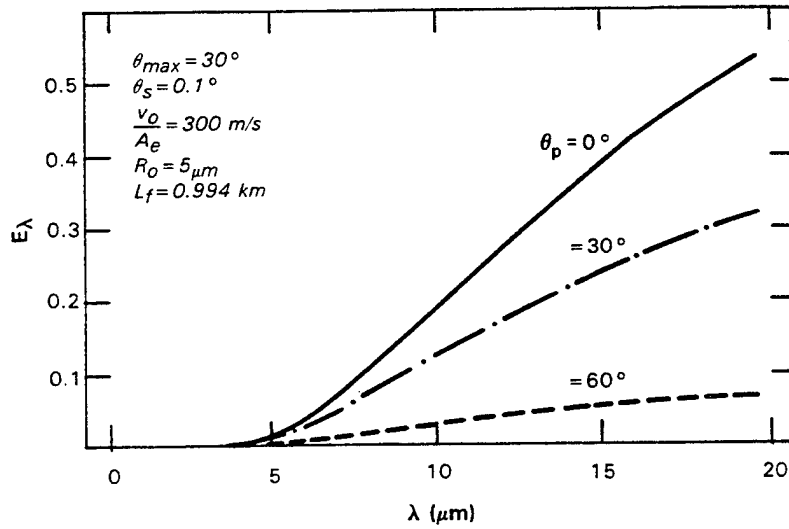


Figure 3-15 Graph of E_λ versus λ for $s = 100 \text{ km}$, $\theta_{max} = 30^\circ$, $\theta_s = 0.1^\circ$, $v_0/A_e = 300 \text{ m/s}$, $R_0 = 5 \mu\text{m}$, and $L_f = 0.994 \text{ km}$.

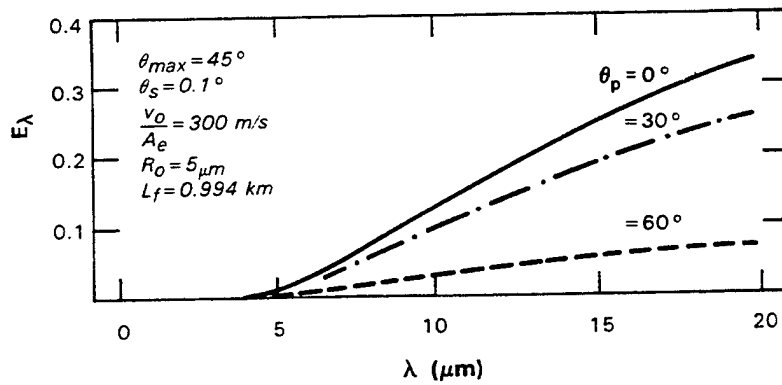


Figure 3-16 Graph of E_λ versus λ for $s = 100 \text{ km}$, $\theta_{max} = 45^\circ$, $\theta_s = 0.1^\circ$, $v_0/A_e = 300 \text{ m/s}$, $R_0 = 5 \mu\text{m}$, and $L_f = 0.994 \text{ km}$.

4. APPLICATION OF THE MODEL TO EXPERIMENTAL DATA

Figure 4-1 shows the basic experimental setup used for Burns 6, 7, and 8 of the March 1988 test series. The flares were mounted at the top of the space chamber and aligned so that the central axis of their exhaust plumes pointed vertically downward. Silicon photometers (sensitive to wavelengths between 0.4 and 1.1 μm) were mounted along the central axis of the exhaust plumes at 3 different stations: 10, 30, and 91 cm from the flare. A 2-channel, Inframetrics radiometer created a pair of video images of about the first 2 m of the flare exhaust plume. The channel 1 video image came from IR radiation with wavelengths between 2.6 and 3.5 μm , and the channel 2 video image from IR radiation with wavelengths between 8 and 12 μm . Selected frames were digitized, corrected for perspective, and compared to a calibrated black-body source to estimate the radiant power emitted per unit length of the plume as a function of distance down its

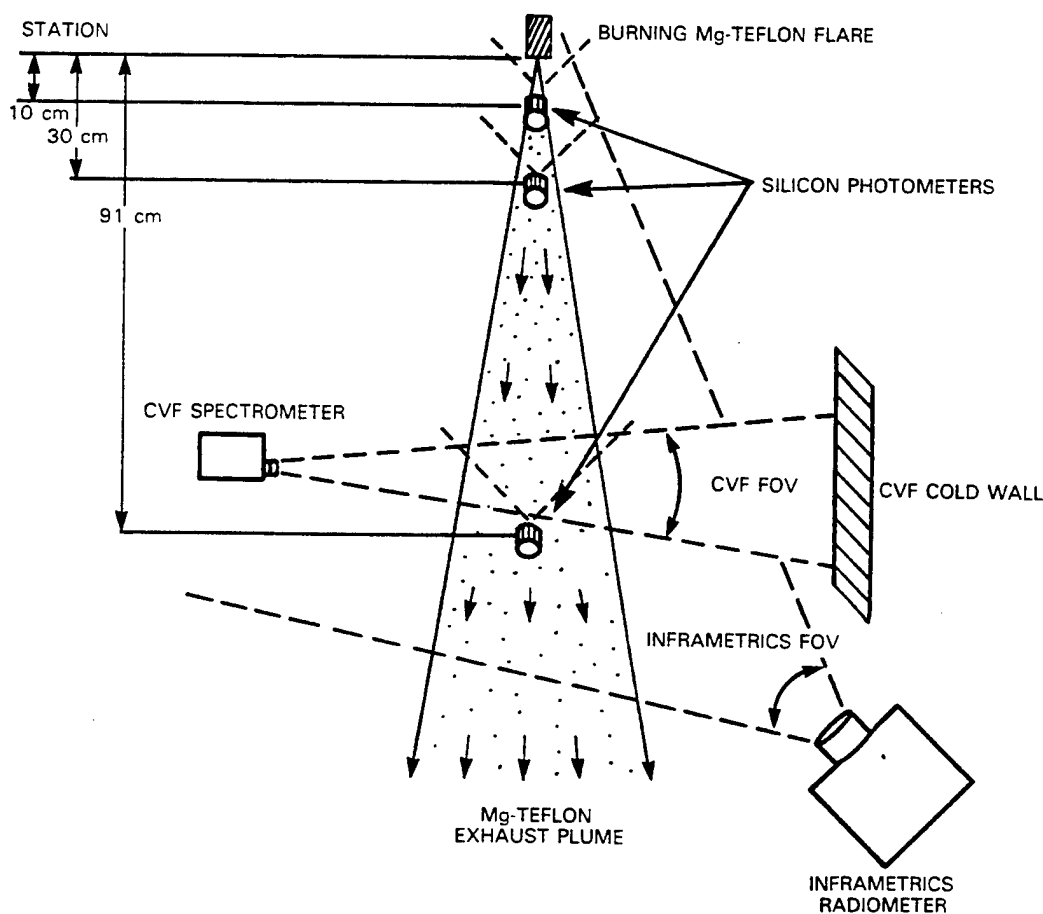


Figure 4-1. Experimental setup used in the March 1988 test series.

central axis. At the 91-cm station, a helium-cooled, circular variable filter (CVF) spectrometer viewed the exhaust plume against a liquid-nitrogen-cooled, cold-wall background. The spectrometer required 1.2 s to scan the wavelengths between 5 and 22.5 μm . A typical burn lasted long enough to provide between 3 and 5 complete spectral scans. Although the formula for $G(\lambda, r)$ given in Equation (2.17) is for a spherical shell of radius r (and thickness dr) centered on the flare, the radiometer estimates of radiant power are directly related to G if, as was the case for Burns 6, 7, and 8, the plume spread angle θ_{max} is small, and r is the distance down the central axis of the plume (see Figure 2-5). If a function \mathcal{G} is defined such that

$$\mathcal{G}(\lambda_a, \lambda_b) = \int_{\lambda_a}^{\lambda_b} G(\lambda, r) d\lambda \quad , \quad (4.1)$$

it follows that channel 1 of the radiometer measured $\mathcal{G}(2.6 \mu\text{m}, 3.5 \mu\text{m})$ and channel 2 measured $\mathcal{G}(8 \mu\text{m}, 12 \mu\text{m})$ as functions of r .

The output of the photometer 10 cm from the flare was correlated with the output of the photometer 30 cm from the flare to measure how fast the exhaust particles were traveling down the plume. The fluctuating plume intensity seen by the 10-cm photometer was labeled "signal A"; that seen by the 30-cm photometer was labeled "signal B." In the notation of our model, v_0 is the average velocity of the Mg-Teflon exhaust plume particles. Fluctuations in signal A are almost certainly caused by clumps of exhaust particles traveling through the 10-cm photometer FOV, and are usually followed by similar fluctuations in signal B after a time lag $\tau = D/v_0$ (where $D = 0.2 \text{ m}$, the distance between the 2 photometer FOVs along the plume central axis). Thus finding the time lag τ which most closely correlates the A and B signal traces is equivalent to finding the value of $v_0 = D/\tau$. Note that this velocity measurement automatically singles out those particles which generate the bulk of the radiant energy coming from the flare exhaust plume.

In Burns 6, 7, and 8, 0.107-s matched sections of the A and B signals were sampled at 17.5- μs intervals. Thus, each 0.107 s section of signal was turned into a data set of $2N$ digitized signal values, N from signal A and N from signal B. Each data set had a slightly different value of N , with $6100 \leq N \leq 6200$ for every digitized data set created. We define A_i, B_i , for $i = 0, 1, \dots, N-1$, to be the $2N$ sampled signal values belonging to a given data set. Thus, A_0, B_0 would be the first A and B signal samples of the data set, A_1, B_1 would be the A and B signal samples 17.5 μs later, and so on. For each data set, a cross-covariance function V_j was defined such that

$$V_j = \begin{cases} \frac{1}{N-|j|} \sum_{i=j}^{N-1} (A_{i-j} - \langle A \rangle) \cdot (B_i - \langle B \rangle) & \text{for } j \geq 0 \\ \frac{1}{N-|j|} \sum_{i=0}^{N-|j|-1} (A_{i+|j|} - \langle A \rangle) \cdot (B_i - \langle B \rangle) & \text{for } j < 0 \end{cases} \quad (4.1a)$$

where

$$j = -2000, -1999, \dots, -1, 0, 1, \dots, 1999, 2000;$$

$$\langle A \rangle = \frac{1}{N} \sum_{i=0}^{N-1} A_i \quad ;$$

$$\langle B \rangle = \frac{1}{N} \sum_{i=0}^{N-1} B_i \quad ;$$

The cross-correlation function C_j is defined in the usual way as

$$C_j = \frac{V_j}{\sqrt{a_0 b_0}} \quad (4.2b)$$

where

$$a_0 = \frac{1}{N} \sum_{i=0}^{N-1} (A_i - \langle A \rangle)^2 \quad ,$$

$$b_0 = \frac{1}{N} \sum_{i=0}^{N-1} (B_i - \langle B \rangle)^2 \quad .$$

When the graphs of C_j versus j for all the data sets were examined, about half contained recognizable peaks marking the time lag which most accurately correlated the A and B signals. Figure 4-2 shows the C_j versus j graph (from Burn 8) which has the most prominent peak found in our cross-correlation calculations, and Figure 4-3 shows the C_j versus j graph (from Burn 7) which has the least prominent peak that was treated as a valid velocity measurement. Table 4-1 gives the average velocity measurements for Burns 6, 7, and 8. Since roughly half the data sets contain recognizable peaks, this is a good indication that our model has made a reasonable approximation of reality when it assigns all the exhaust particles in the flare plume the same average velocity v_0 .

The output of the 10-cm-station photometer was used to estimate the flare combustion rate P . The area under the photometer intensity curve is assumed to be proportional to the total amount of fuel burned by the flare. Estimates were made of the rectangular area that would be equal to the actual area under each curve given the constraint that the top level of the rectangle be equal in height to the quasi-steady intensity level characterizing the middle portion of each burn. By dividing the length of each rectangle (representing a time interval in seconds) into the amount of fuel burned by each flare, estimates can be made of the actual combustion rate P characterizing the quasi-steady intensity levels of Burns 6, 7, and 8 (see Figure 4-4).

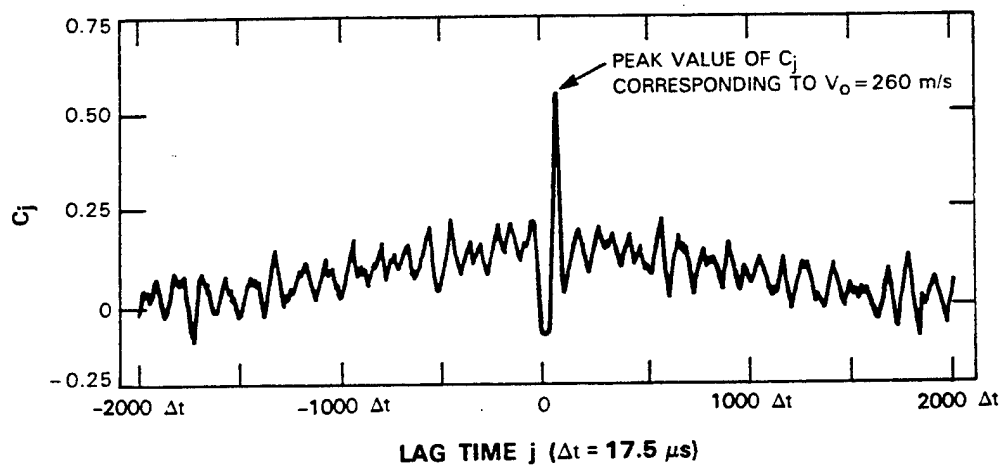


Figure 4-2. Graph of C_j versus j from Burn 8 at 2.9 s after ignition.

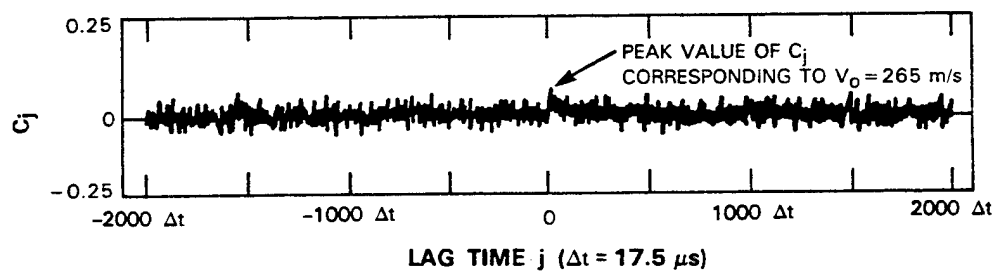


Figure 4-3. Graph of C_j versus j from Burn 7 at 2.5 s after ignition.

<p style="text-align: center;">TABLE 4-1 Average Velocities From Photometer Correlations Over Intervals of 0.107 s</p>			
	Burn 6 (m/s)	Burn 7 (m/s)	Burn 8 (m/s)
Average	223.5	238	273
Standard Deviation	47	28	47
Number of Velocity Measurements	6	4	9

A pyrotechnic flare with a chemical composition similar to that of Burns 6, 7, and 8 was burned inside the space chamber in such a way that its exhaust plume passed through the measuring volume of a Malvern particle sizer. The particle sizer measured $D(4,3)$ and $D(3,2)$ for the collection of particles in the exhaust plume, where

$$D(4,3) = 2 \cdot \int_0^\infty R^4 f(R) dR / \int_0^\infty R^3 f(R) dR = 7.4 \mu\text{m} \quad (4.3a)$$

$$D(3,2) = 2 \cdot \int_0^\infty R^3 f(R) dR / \int_0^\infty R^2 f(R) dR = 4.9 \mu\text{m} \quad (4.3b)$$

Substitute Equation (2.2) into (4.3a,b) and solve for σ and R_{1a} .

$$\sigma = \sqrt{\ln[D(4,3)/D(3,2)]} = 0.64 \quad (4.4a)$$

$$R_{1a} = \frac{1}{2} [D(3,2)]^{7/2} / [D(4,3)]^{5/2} = 0.87 \mu\text{m} \quad (4.4b)$$

This completely specifies the size distribution $f(R)$ defined in Equation (2.2) and used inside the integral in Equation (2.17). There is a significant spread in this log-normal distribution; the average value of R is $1.1 \mu\text{m}$ while the most probable value of R is $0.58 \mu\text{m}$.

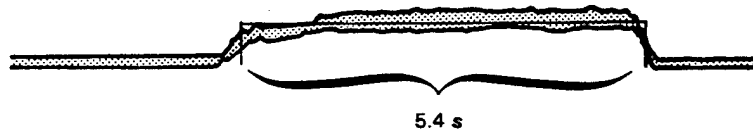
For five different r values (0.1, 0.25, 0.50, 0.75, and 1 m) we calculated the average values of $\mathcal{G}(2.6 \mu\text{m}; 3.5 \mu\text{m})$ and $\mathcal{G}(8 \mu\text{m}, 12 \mu\text{m})$ using selected video frames from the quasi-steady portions of Burns 6, 7, and 8. These experimental values of \mathcal{G} are presented in Tables 4-2, 4-3, and 4-4. Since the entire collection of video frames was not averaged, when the average of the sampled frames is calculated it may, due to the luck of the draw, differ from the true average by a significant amount. There are well-known formulas which can be used to calculate the standard deviation of this sort of sampling error, and the percentage values of the normalized statistical error given in Tables 4-2, 4-3, and 4-4 are just this standard deviation divided by \mathcal{G} . The values of G/P in these tables come from the measured \mathcal{G} values being divided by the combustion rate P (given

BURN 6



FLARE WEIGHT = 8.94 gm; BURN RATE = $P = 2.6$ gm/s

BURN 7



FLARE WEIGHT = 8.16 gm; BURN RATE = $P = 1.5$ gm/s

BURN 8



FLARE WEIGHT = 8.90 gm; BURN RATE = $P = 2.3$ gm/s

Figure 4-4 Graph of the photometer signal (10-cm station) versus time for Burns 6, 7, and 8.

107853-27

TABLE 4-2 Average Radiance Values versus Distance Down the Plume for Burn 6 of March 1988 Test Series		
Channel 1 ($2.6 \leq \lambda \leq 3.5 \mu\text{m}$)		
r in m	G/p in $\frac{\text{w/sr/m}^2}{\text{kg/s}}$	\mathcal{G} in w/sr/m*
0.1	2.02×10^{10}	47.2
0.25	1.61×10^{10}	37.6
0.50	1.11×10^{10}	26.0
0.75	8.59×10^9	20.1
1.00	6.67×10^9	15.6
Channel 2 ($8 \leq \lambda \leq 12 \mu\text{m}$)		
r in m	G/p in $\frac{\text{w/sr/m}^2}{\text{kg/s}}$	\mathcal{G} in w/sr/m*
0.1	5.88×10^8	6.11
0.25	6.50×10^8	6.76
0.50	5.75×10^8	5.98
0.75	4.60×10^8	4.78
1.00	3.77×10^8	3.92

*Statistical error in G/p and \mathcal{G} is ≤ 4 percent

<p align="center">TABLE 4-3</p> <p align="center">Average Radiance Values versus Distance Down the Plume</p> <p align="center">for Burn 7 of March 1988 Test Series</p>		
Channel 1 ($2.6 \leq \lambda \leq 3.5 \mu\text{m}$)		
r in m	G/p in $\frac{\text{w/sr/m}^2}{\text{kg/s}}$	\mathcal{G} in w/sr/m*
0.1	2.07×10^{10}	28.1
0.25	1.62×10^{10}	22.0
0.50	1.17×10^{10}	15.9
0.75	9.49×10^9	12.9
1.00	7.73×10^9	10.5
Channel 2 ($8 \leq \lambda \leq 12 \mu\text{m}$)		
r in m	G/p in $\frac{\text{w/sr/m}^2}{\text{kg/s}}$	\mathcal{G} in w/sr/m*
0.1	7.12×10^8	4.30
0.25	7.09×10^8	4.28
0.50	6.56×10^8	3.96
0.75	4.55×10^8	2.75
1.00	3.99×10^8	2.41

*Statistical error in G/p and \mathcal{G} is ≤ 5 percent

TABLE 4-4 Average Radiance Values versus Distance Down the Plume for Burn 8 of March 1988 Test Series		
Channel 1 ($2.6 \leq \lambda \leq 3.5 \mu\text{m}$)		
r in m	G/p in $\frac{\text{w/sr/m}^2*}{\text{kg/s}}$	\mathcal{G} in w/sr/m*
0.1	1.72×10^{10}	35.7
0.25	1.34×10^{10}	27.7
0.50	9.52×10^9	19.7
0.75	7.15×10^9	14.8
1.00	5.56×10^9	11.5
Channel 2 ($8 \leq \lambda \leq 12 \mu\text{m}$)		
r in m	G/p in $\frac{\text{w/sr/m}^2*}{\text{kg/s}}$	\mathcal{G} in w/sr/m*
0.1	5.59×10^8	5.14
0.25	5.41×10^8	4.98
0.50	4.82×10^8	4.43
0.75	3.43×10^8	3.16
1.00	2.92×10^8	2.69

*Statistical error in G/p and \mathcal{G} is ≤ 7 percent

in Figure 4-4) and the associated wavelength interval ($0.9 \mu\text{m}$ for channel 1 and $4 \mu\text{m}$ for channel 2). The \mathcal{G} values in Tables 4-2, 4-3, and 4-4 have been plotted in Figures 4-5, 4-6, and 4-7 with error bars representing the un-normalized standard deviation of the sampling error for each value of \mathcal{G} and r .

The solid lines in Figures 4-5, 4-6, and 4-7 present the best least-squares fit of the model specified by Equations (2.2), (2.11), (2.12), (2.17), and (2.18) to the G/P values given in Tables 4-2, 4-3, and 4-4. (Finding the best least-squares fit to the \mathcal{G} values themselves would have taken an inordinate amount of computer time.) Having written a computer program to calculate the predicted G/P values using these 5 equations, it was found that the model values depend on the 7 free parameters A_e , σ , ρ , v_o , R_{la} , C_p and T_o . The 2 basic products of Mg-Teflon combustion are carbon and magnesium fluoride, so ρ , the mass density of the exhaust particles, is set equal to 2.6 gm/cm^3 , the average of the mass densities of carbon and magnesium fluoride. The value of v_o comes from Table 4-1, and the values of σ and R_{la} have been calculated in Equation (4-4a,b). Thus, in the least-squares fit, we adjust the 3 remaining parameters A_e , C_p , and T_o to fit the 10 data points in Tables 4-2, 4-3, and 4-4 to find that

$$T_o = \begin{cases} 1587^\circ\text{K} & \text{for Burn 6} \\ 1561 & 7 \\ 1662 & 8 \end{cases} \quad (4.5)$$

$$C_p = \begin{cases} 1.63 \times 10^3 \text{ J/kg/}^\circ\text{K} & \text{for Burn 6} \\ 1.81 & 7 \\ 1.20 & 8 \end{cases} \quad (4.6)$$

$$A_e = \begin{cases} 1.90 \text{ (dimensionless)} & \text{for Burn 6} \\ 2.23 & 7 \\ 1.88 & 8 \end{cases} \quad (4.7)$$

The flame temperature of a chemical reaction is the predicted temperature of its products given that all the energy generated by the reaction is absorbed by the products as heat. In Equation (4.5) the values of T_o , the temperature at which the exhaust particles leave the flare, compare well to the predicted flame temperature (about 2000°K) of the Mg-Teflon mixture used in these 3 burns. On the one hand, they are somewhat less than the flame temperature, which makes sense because the flares are not adiabatically isolated thermodynamic systems; yet on the other hand, they are not so much smaller as to cast doubt on the model's basic validity. As for the values of C_p shown in Equation (4.6), they too seem reasonable, given that the C_p of pure magnesium difluoride is $1.21 \times 10^3 \text{ J/kg/}^\circ\text{K}$ (the C_p of carbon has a pronounced temperature dependence, yet at these temperatures its C_p is the same order of magnitude as that of magnesium difluoride). As for A_e in Equation (4.7), it is indeed of $O(1)$ as required by our model. Clearly, the best least-squares fit of theory to data does not require the 3 adjustable parameters T_o , C_p , and A_e to take on unphysical values.

The error bars in Figures 4-5, 4-6, and 4-7 represent the standard deviation of the statistical sampling error, and it can be seen that, by and large, the channel 1 predicted radiance curves lie within the error bars of the experimental data for Burns 6, 7, and 8. However just the opposite

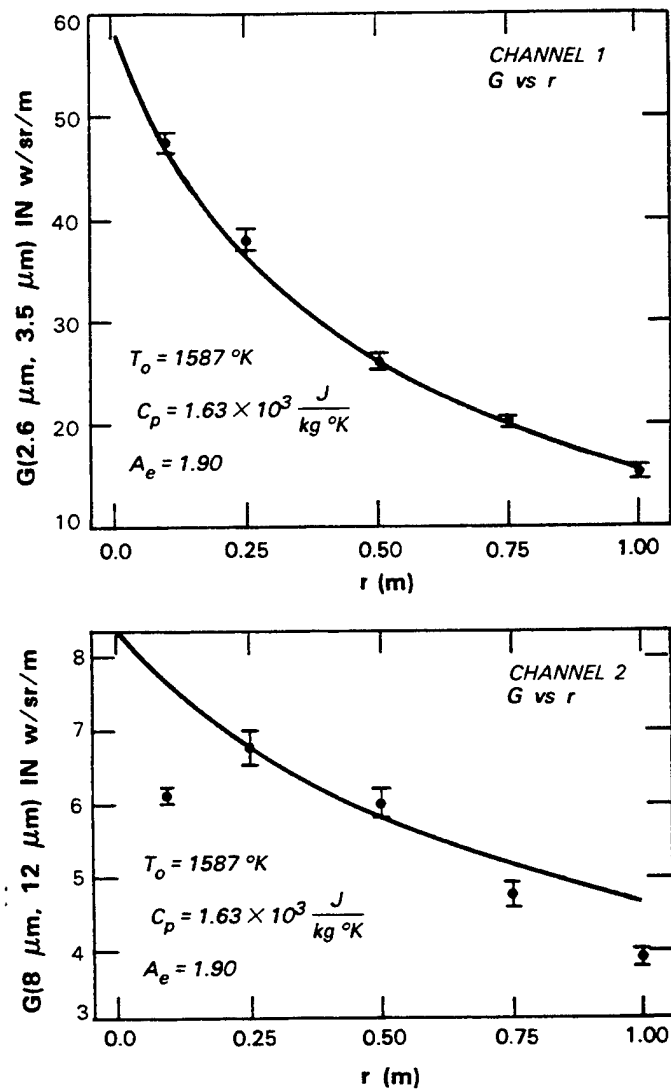


Figure 4-5. Graph of average radiant intensity versus distance down the plume for Burn 6.

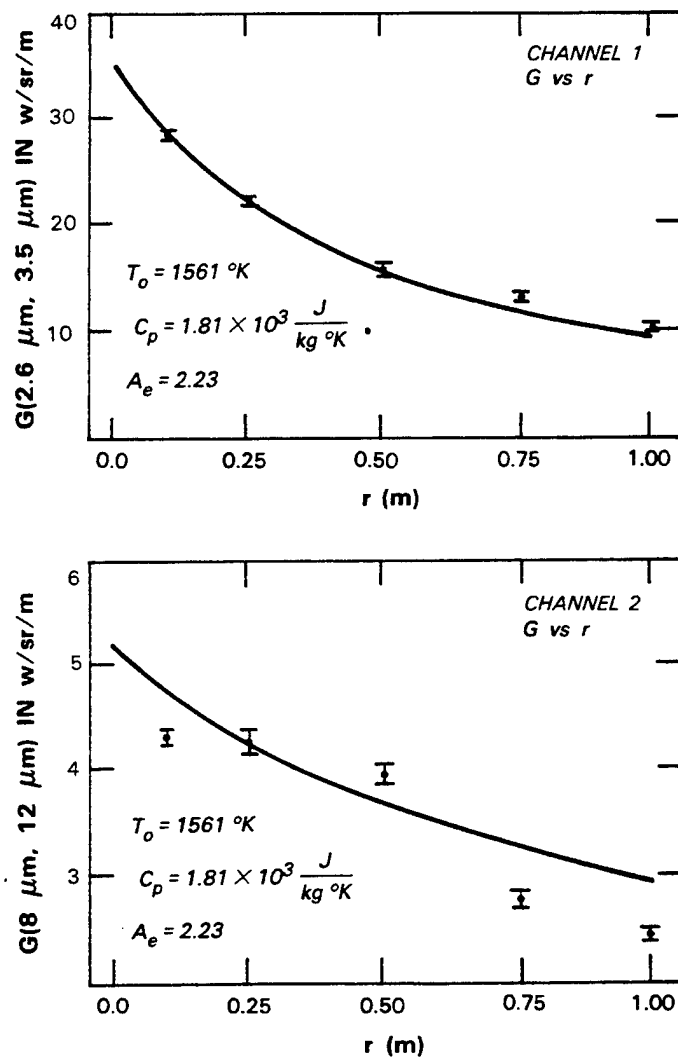


Figure 4-6. Graph of average radiant intensity versus distance down the plume for Burn 7.

107853-29

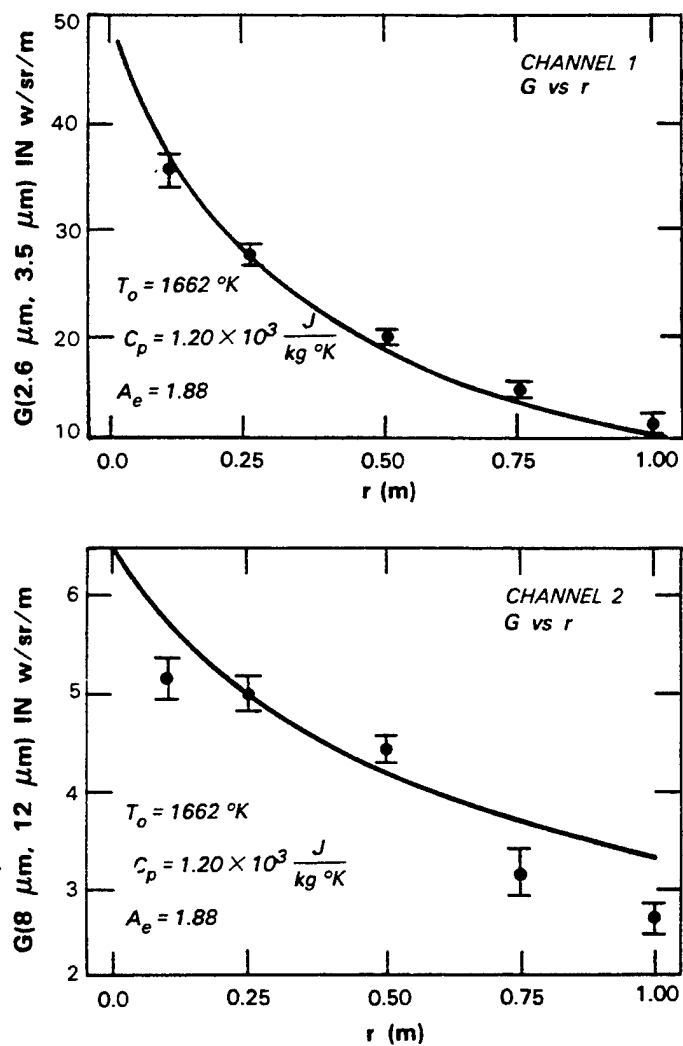


Figure 4-7. Graph of average radiant intensity versus distance down the plume for Burn 8.

can be said about the channel 2 predicted radiance curves; they, as a general rule, lie well outside the error bars of the experimental data. The best way to understand this is to remember that the statistical sampling error is just the random component of the experimental error; the total experimental error could be much larger due to systematic inaccuracies in the experimental apparatus. In fact, the general shape of the channel 2 radiance data is inherently implausible. In Burn 6, the channel 2 radiance increases substantially going from $r = 0.1$ to 0.25 m; and in Burns 7 and 8, although the radiance decreases, the amount of the decrease seems anomalously low. Furthermore, although Table 4-5 shows that the channel 1 radiance values are more or less confirmed by the photometer output, Table 4-6 shows that the CVF spectrometer mounted at the 91-cm station in Figure 4-1 is consistently in disagreement with the channel 2 radiance values. (The channel 2 radiance is for wavelengths between 8 and $12\text{ }\mu\text{m}$; Table 4-6 compares the channel 2 radiance to the CVF integrated spectral intensity from 8 to $12\text{ }\mu\text{m}$.) If the disagreement between the CVF spectrometer and the Inframetrics radiometer is taken to be a measure of the total channel 2 error, the channel 2 data are found to be in error by 20 to 30 percent. If the error bars were to be extended by this amount in the channel 2 graphs of Figures 4-5, 4-6, and 4-7, all the channel 2 experimental data, like that of channel 1, would match the predicted radiance curves. It is thus tentatively concluded that the model radiance equations derived above adequately describe, to within experimental error, the radiance profile of Mg-Teflon flares burning in a vacuum.

<p align="center">TABLE 4-5</p> <p align="center">Comparison of Inframetrics Radiometer Channel 1 Readings to 91-cm Station Photometer for March 1988 Test Series</p>		
Burn Number	Inframetrics Channel 1	Photometer
1	0.05 w/cm/sr/ μ	0.05 w/cm/sr/ μ
2	0.10	0.08
3	0.06	0.05
4	(instrument failure)	(instrument failure)
5	0.18	0.17
6	0.13	0.11
7	0.09	0.08
8	0.11	0.12
9	0.16	0.11
10	0.14	0.12

TABLE 4-6 Comparison of Inframetrics Radiometer Channel 2 Readings to 91-cm Station CVF Spectrometer for March 1988 Test Series		
Burn Number	Inframetrics Channel 2	CVF Spectrometer
1	$1.1 \times 10^{-4} \text{ w/cm}^2/\text{sr}/\mu$	$1.1 \times 10^{-4} \text{ w/cm}^2/\text{sr}/\mu$
2	5.0×10^{-4}	1.9×10^{-4}
3	1.3×10^{-4}	0.8×10^{-4}
4	(instrument failure)	(instrument failure)
5	5.0×10^{-4}	2.7×10^{-4}
6	4.4×10^{-4}	3.3×10^{-4}
7	2.9×10^{-4}	2.3×10^{-4}
8	3.3×10^{-4}	2.4×10^{-4}
9	3.9×10^{-4}	2.5×10^{-4}
10	3.5×10^{-4}	2.0×10^{-4}

5. CONCLUSIONS

A model was constructed to predict the IR radiant intensity of particulate exhaust plumes generated by pyrotechnic flares burning in a vacuum. In this model, it was assumed that the exhaust plume particles come in a variety of sizes described by a log-normal probability density distribution, that the particles all travel at the same average velocity, and that the particles do not absorb or scatter significant amounts of radiation — that is, that the plume is optically thin. Both the geometric irregularity and the lack of chemical purity of the exhaust plume particles have been acknowledged by using a phenomenological approximation, rather than Mie theory, to describe the dependence of particle grey-body emissivity on particle size. A single-size version of this model (where all the exhaust particles have the same radius value) has been used to predict what the exhaust plume of a Mg-Teflon flare would look like when viewed as an approximate point source by a distant IR sensor. The IR radiance data taken from three separate Mg-Teflon flares burned in the space chamber were also compared to what the multisize version of our model (where particle radius values obey a log-normal probability density function) predicted should occur. The single-size model gave a reasonable description of a Mg-Teflon flare viewed as a distant source of IR radiation, and the multisize model predictions matched the space-chamber data to within estimated experimental error. Clearly, the approximations used to construct the model are a reasonable description of reality, and the model itself is a useful tool for understanding the exhaust plumes of pyrotechnic flares burning in a vacuum.

REFERENCES

1. T. Allen, *Particle Size Measurement*, New York: John Wiley and Sons (1975), pp. 74-85.
2. C.F. Bohren and D.R. Huffman, *Absorption and Scattering of Light by Small Particles*, New York: John Wiley and Sons (1983), pp. 125 and 136.

BIBLIOGRAPHY

1. J. Aitchison and J.A.C. Brown, *The Lognormal Distribution*, New York: Cambridge University Press (1969).
2. G. Bauer, *Measurement of Optical Radiations*, New York: The Focal Press (1962).
3. M.W. Beckstead and E.W. Price, "Nonacoustic Combustion Instability," *AIAA J.*, 5, 1989 (1967).
4. S. Chandrasekhar, *Radiative Transfer*, New York: Dover Publications, Inc. (1972).
5. W.H. Dalzell and A.F. Sarofim, "Optical Constants of Soot and Their Application to Heat-Flux Calculations," *J. Heat Transfer*, 91, 100 (1969).
6. J.V. Dave, "Scattering of Electromagnetic Radiation by a Large, Absorbing Sphere," *IBM J. Res. Dev.*, 302 (1969).
7. J.M. Dowling and C.M. Randall, *Infrared Emissivities of Micro-Sized Particles of C, MgO, Al₂O₃ and ZrO₂ at Elevated Temperatures*, AFRPL-TR-77-14 (1977).
8. E.R.G. Eckert and R.M. Drake, Jr., *Analysis of Heat and Mass Transfer*, New York: McGraw-Hill Book Company, (1972).
9. D.K. Edwards and R.P. Bobco, "Effect of Particle Size Distribution on the Radiosity of Solid Propellant Rocket Motor Plumes," AIAA-81-1052, AIAA 16th Thermophysics Conference.
10. B. Epstein, "The Mathematical Description of Certain Breakage Mechanisms Leading to the Logarithmico-Normal Distribution," *J. Franklin Inst.*, 224, 471 (1947).
11. P. Faraday, "Forward Light Diffraction Techniques for Drop Size Analysis," Filtech Conference 1983.
12. J.R. Fincke, C.L. Jeffery, and R. E. Spjut, "Measurement of the Emissivity of Small Particles at Elevated Temperatures," *Opt. Eng.*, 27, 684 (1988).
13. J.E. Fontenot, "Thermal Radiation from Solid Rocket Plumes at High Altitude," *AIAA J.*, 3, 970 (1965).
14. J. R. Hodkinson, "Refractive Index and Particle-Extinction Efficiency Factors for Carbon," *J. Opt. Soc. Am.*, 54, 846 (1964).

15. G.M. Jenkins and D.G. Watts, *Spectral Analysis*, San Francisco: Holden-Day, Inc. (1968).
16. G. W. Kattawar and M. Eisner, "Radiation from a Homogeneous Isothermal Sphere," *Appl. Opt.*, **9**, 2685 (1970).
17. B.H. Kaye, *Direct Characterization of Fine Particles*, New York: John Wiley and Sons (1981).
18. M. Kerker, *The Scattering of Light and Other Electromagnetic Radiation*, New York: Academic Press (1969).
19. K.K. Kuo and M. Summerfield, eds., "Fundamentals of Solid-Propellant Combustion" *Prog. Astronaut. and Aeronaut.*, **90** (1984).
20. K.W. Lee, H. Chen, and J.A. Grieseke, "Log-Normally Preserving Size Distribution for Brownian Coagulation in the Free-Molecule Regime," *Aerosol Science and Technology*, **3**, 53 (1984).
21. A.R. Nagy, Jr., and J.M. Lenoir, "Absorption and Scattering of Thermal Radiation by a Cloud of Small Particles," *AIChE J.*, **16**, 286 (1970).
22. M.N. Ozisik, *Radiative Transfer and Interactions with Conduction and Convection*, New York: John Wiley and Sons, Inc. (1973).
23. A.B. Pluchino, S.S. Goldberg, J.M. Dowling, and C.M. Randall, "Refractive-Index Measurements of Single Micron-Sized Carbon Particles," *Appl. Opt.*, **19**, 3370 (1980).
24. W.S. Rothwell and H.L. Schick, "Emission Spectra from a Stream of Cooling Particles," *J. Spacecr.*, **11**, 597 (1974).
25. T. Sato and R. Matsumoto, "Radiant Heat Transfer from Luminous Flame," *Amer. Soc. Mech. Eng.*, 804 (1963).
26. D.W. Schuerman, ed., *Light Scattering by Irregularly Shaped Particles*, New York: Plenum Press (1980).
27. E.M. Sparrow and R.D. Cess, *Radiation Heat Transfer*, New York: McGraw-Hill Book Company (1978).
28. J.D. Stockham and E.G. Fochtman, eds., *Particle Size Analysis*, Ann Arbor, Mich.: Ann Arbor Science Publishers, Inc., (1979).
29. V.R. Stull and G.N. Plass, "Emissivity of Dispersed Carbon Particles," *J. Opt. Soc. Am.*, **50**, 121 (1960).
30. H.C. Van De Hulst, *Light Scattering by Small Particles*, New York: John Wiley and Sons (1983).
31. B.W. Worster, "Particulate Infrared Radiation in Aluminized Solid-Fuel Rocket Plumes," *J. Spacecr.*, **11**, 260 (1974).

REPORT DOCUMENTATION PAGE

Form Approved
OMB No. 0704-0188

Public reporting burden for this collection of information is estimated to average 1 hour per response, including the time for reviewing instructions, searching existing data sources, gathering and maintaining the data needed, and completing and reviewing the collection of information. Send comments regarding this burden estimate or any other aspect of this collection of information, including suggestions for reducing this burden, to Washington Headquarters Services, Directorate for Information Operations and Reports, 1215 Jefferson Davis Highway, Suite 1204, Arlington, VA 22202-4302, and to the Office of Management and Budget, Paperwork Reduction Project (0704-0188), Washington, DC 20503.

1. AGENCY USE ONLY (Leave blank)		2. REPORT DATE 17 March 1989 Reissued 3/29/2000	3. REPORT TYPE AND DATES COVERED Technical Report	
4. TITLE AND SUBTITLE A Model for the Infrared Radiance of Optically Thin, Particulate Exhaust Plumes Generated by Pyrotechnic Flares Burning in a Vacuum			5. FUNDING NUMBERS C — F19628-85-C-0002	
6. AUTHOR(S) Douglas L. Cohen				
7. PERFORMING ORGANIZATION NAME(S) AND ADDRESS(ES) Lincoln Laboratory, MIT 244 Wood Street Lexington, MA 02420-9108			8. PERFORMING ORGANIZATION REPORT NUMBER TR-821	
9. SPONSORING/MONITORING AGENCY NAME(S) AND ADDRESS(ES) Ballistic Missile Office, USAF Electronic Systems Division Norton AFB, CA 92409 Hanscom AFB, MA 01731			10. SPONSORING/MONITORING AGENCY REPORT NUMBER ESD-TR-88-223	
11. SUPPLEMENTARY NOTES None				
12a. DISTRIBUTION/AVAILABILITY STATEMENT Approved for public release; distribution is unlimited.			12b. DISTRIBUTION CODE	
13. ABSTRACT (Maximum 200 words) This report sets up a model for the intensity of infrared radiation emitted by a particulate exhaust plume generated by a pyrotechnic flare burning in a vacuum. The model assumes that the exhaust plume is optically thin, that it is composed mostly of discrete particles, that the particles have a size spectrum described by a log-normal probability density function, that they cool off entirely by the emission of thermal radiation, and that they all travel at the same average velocity. The model is used to predict how a magnesium-Teflon exhaust plume would look when viewed as an approximate point source by a distant infrared sensor and also to analyze the data acquired from three separate magnesium-Teflon flares burned in a large vacuum chamber.				
14. SUBJECT TERMS infrared radiance particulate exhaust plumes vacuum-burning flare			15. NUMBER OF PAGES 62	
			16. PRICE CODE	
17. SECURITY CLASSIFICATION OF REPORT Unclassified	18. SECURITY CLASSIFICATION OF THIS PAGE Unclassified	19. SECURITY CLASSIFICATION OF ABSTRACT Unclassified	20. LIMITATION OF ABSTRACT Same as Report	